INTERNATIONAL JOURNAL FOR NUMERICAL METHODS IN FLUIDS, VOL. 16, 1 27 (1993)

NAVIER–STOKES COMPUTATIONS PAST A PROLATE SPHEROID AT INCIDENCE. II: HIGH INCIDENCE CASE

J. PIQUET AND P. QUEUTEY

CFD Group, LMF-URA 1217 CNRS, ECN, 1 Rue de la Noe, 44072 Nantes Cedex, France

SUMMARY

The computation of incompressible three-dimensional viscous flow is investigated. An iterative fully decoupled technique based on the fully elliptic mode is applied to the Reynolds-averaged-Navier–Stokes equations (RANSE) written down in a non-orthogonal curvilinear body-fitted co-ordinate system. Results of the computations are compared with experimental data past a prolate spheroid at 30° incidence.

KEY WORDS Finite volume Navier–Stokes equations Collocative methods Prolate spheroid

1. INTRODUCTION

Vortical motions that will be discussed in the following result from the geometry of the body which packs the boundary layer into an area whose girthwise dimension decreases. External flow streamlines are, thus, made to converge rapidly in planes parallel to the surface. Then, continuity requires a large normal velocity, i.e. a large upward bend of the streamlines. This in turn creates a large normal pressure gradient towards the surface where the pressure is increased. These characteristics are connected to a dramatic thickening of the boundary layer which strongly interacts with the external inviscid flow. The actual wall pressure distribution differs significantly from that calculated by the potential flow theory, while the static pressure varies across the viscous zone. In the case of slender geometries, like ship hulls, fuselages or missiles at incidence, the strong viscous–inviscid interaction occurs with boundary layer separation. While the boundary layer remains attached for about 90% of the body length at low angles of attack (say 10°), experimental results indicate that for high incidences, a longitudinal vortex motion promotes massive boundary layer separation and rolling up of vortex sheets on the leeward side of the body. The ability of Reynolds-averaged-Navier–Stokes equations (RANSE) to describe such a strongly concentrated vortical flow is demonstrated for one benchmark example, namely the 6:1 prolate spheroid at 30° incidence and a Reynolds number of $7{\cdot}2\times10^6$.

Such a case is interesting not only in its own right but also because it exhibits the previously mentioned complex flow phenomena on a particularly simple geometry. Also, the problem involves an analytical potential-flow solution. However, for the present high-incidence case with massive separation, this solution is valid only on the windside region close to the attachment node. Finally, detailed experimental measurements have been performed by Meier *et al.*;[1–4] they include surface shear stresses, pressures and oil flows.

In contrast to the 10° incidence case, reviewed in Reference 5, which has often been studied, only a few comparisons are available for the 30° case. Some conventional boundary layer calculations[6–8] are available with a Cebeci–Smith model of turbulence. However, they cover only a small region of the boundary layer. Some thin-layer Navier–Stokes calculations using

0271–2091/93/010001–27$18.50

Received October 1991
Revised April 1992

a Baldwin–Lomax model of turbulence are also presented.[9–11] They are very similar in that an approximate factorization of Beam and Warming type is used, with diagonalized implicit operators and dependent variables written in their incremental form. As a result, pentadiagonal matrices with fourth-order dissipation have to be solved. The method[9] compares the results of two different procedures which use the same centred differences for viscous fluxes. For inviscid fluxes, two different finite volume schemes are compared: the first one is a flux difference splitting scheme of Roe type in which the Jacobian matrices of the inviscid fluxes are split backwards and forwards according to the signs of the eigenvalues of the matrices of the inviscid fluxes: upwind differencing here provides the artificial dissipation. The second scheme used also in Reference 11 is based on a multistage Runge–Kutta time-stepping scheme for a space-centred difference method with a controlled, and explicitly added, amount of artificial dissipation. The outputs of the resulting code (CFL3D) are compared in Reference 10 with those of a different code (VOR3DI) which is based on the so-called pseudo-compressibility approach, following Reference 12.

2. THE EQUATIONS

2.1. *The vector form of the basic equations*

The exact RANSE of continuity and momentum of the mean flow in dimensionless form are given by equations (1a) and (1b):

$$\operatorname{div}\mathbf{U}=0, \tag{1a}$$

$$\frac{\partial\mathbf{U}}{\partial t}+\nabla\cdot\mathbf{U}\mathbf{U}+\nabla p+\nabla\cdot\overline{\mathbf{uu}}=\frac{1}{Re}\nabla^{2}\mathbf{U}, \tag{1b}$$

where $\mathbf{U}$, p and $\overline{\mathbf{uu}}$ are, respectively, the velocity vector, the pressure and the Reynolds stress tensor. The resulting turbulent closure problem is solved by means of an algebraic viscosity model in which the Reynolds stress is linearly related to the mean rate of strain tensor through an isotropic eddy viscosity as follows:

$$\overline{\mathbf{uu}}=\tfrac{2}{3}\,k\,\mathbf{1}-\nu_{\mathrm{T}}(\nabla\mathbf{U}+\nabla^{\mathrm{T}}\mathbf{U}). \tag{2}$$

A mixing-length model is used where ν_{T} is specified by

$$\nu_{\mathrm{T}}=L^{2}[\nabla\mathbf{U}:(\nabla\mathbf{U}+\nabla^{\mathrm{T}}\mathbf{U})], \tag{3a}$$

where the mixing length L is specified over the whole viscous layer (from the wall to infinity) by

$$L=L_{\infty}[1-\exp(-n^{+}/A^{+})]\tanh(\kappa n/L_{\infty}). \tag{3b}$$

The damping coefficient is $A^{+}=26$, $\kappa=0.41$, n is the normal distance to the body, $n^{+}=nReU_{\tau}$ and L_{∞} is estimated as $0{\cdot}08\delta$, where δ is the thickness of the viscous layer. δ is estimated from the velocity modulus u_{e} at the 'edge' of the layer. u_{e} is estimated as $0{\cdot}995u_{\max}$, if $u_{\max}$ is the maximum of the modulus of the velocity. The effective Reynolds numbers R_{eff} is defined by $R_{\mathrm{eff}}=1/[\nu_{\mathrm{T}}+Re^{-1}]$. Other algebraic models have been also considered, namely the Baldwin and Lomax model[13] with modifications suggested in Reference 14.

2.2. *The equations in the transformed co-ordinate system*

For most practical applications, the complexity of the geometry prevents the use of Cartesian or cylindrical co-ordinate systems. Analytic or numerical co-ordinate transformations are highly desirable in that they greatly facilitate the application of the boundary conditions and transform the physical domain in Ω which the flow is studied into a parallelepipedic computational domain $\{\xi^i\}=\{\xi, \eta, \zeta\}$. The domain Ω becomes a parallelepiped in the computational space in which the discretization consists of stacked unit cubes of sides $\Delta\xi^i=1$, $i=1, 2, 3$. Each unit cube of the computational space is a curvilinear hexahedron in the physical space, the 'sides' of which are measured by the modulii of the covariant vectors $\mathbf{a}_i=\partial\mathbf{r}/\partial\xi^i$.

The transformation necessarily involves by-products from the covariant basis $\mathbf{a}_j$. Of particular interest are[15]:

(i) The area vectors $\mathbf{b}^i=\mathbf{a}_j\times\mathbf{a}_k$ (i, j, k in cyclic order), which measure the oriented area of a small surface of unit sides along ξ^j and ξ^k on a $\xi^i=$constant surface in the computational space. $\mathbf{b}^i$ appears as constructed with two small triangle-like surfaces in the physical space.

(ii) The Jacobian J of the transformation from the computational space of the co-ordinates $\{\xi^i\}$ to the physical space of the Cartesian co-ordinates $\{\bar{x}^\alpha\}$. J measures the 'physical' volume of a parallelepiped of unit sides in the computational space and is evaluated in such a way that $\mathbf{a}_i\cdot\mathbf{b}^j=J\,\delta_i^j$; this parallelepiped appears as an hexaedron-like volume in the physical space.

(iii) The covariant and contravariant metric tensors $g_{ij}=\mathbf{a}_i\cdot\mathbf{a}_j$; $g^{ij}=g^{-1}\,\mathbf{b}^i\cdot\mathbf{b}^j$, where g the determinant of g_{ij}, is the square J^2 of the foredefined Jacobian.

An important relationship to be used is the following simple restatement (3) of the chain-rule derivative formula:

$$\frac{\partial\xi^k}{\partial\bar{x}^\alpha}=J^{-1}\,b^k_\alpha, \tag{4}$$

which allows the computation of the following standard operator:

$$\nabla\cdot\mathbf{U}=J^{-1}\,\frac{\partial(JU^i)}{\partial\xi^i}=J^{-1}\,\frac{\partial[b^i_\alpha\bar{U}^\alpha]}{\partial\xi^i}, \tag{5}$$

where $\bar{U}\alpha$ and $[\overline{\nabla\phi}]_\alpha$ are the physical components in the Cartesian orthonormalized physical space (where contravariant and covariant components are identical so that they can be treated indifferently as subscripts and superscripts). In the following, the summation convention is used systematically, unless specified.

If $\bar{U}^\alpha=\delta^\alpha_\beta$ with $\beta=1$, 2 or 3, equation (4) indicates that

$$\frac{\partial b^i_\beta}{\partial\xi^i}=0 \quad \text{for } \beta=1, 2 \text{ and } 3. \tag{6}$$

Equation (5) is the so-called geometrical conservation law which amounts to the fact that, when properly discretized, areas of a discrete cell will sum to the total volume. Also, the gradient components are given by

$$[\overline{\nabla\phi}]_\alpha=J^{-1}\,b^k_\alpha\,\frac{\partial\phi}{\partial\xi^k}. \tag{7}$$

The curvilinear body-fitted C-type grid is generated using the solution of a set of Poisson equations, in a manner described in Reference 15. The partially transformed RANSE are given by the following relations *in a strongly conservative form.* The contravariant components of the velocity are defined by $\{U^i\}$ and the physical Cartesian components by $\{\bar{U}^\alpha\}$. The continuity equation is (8):

$$\frac{1}{J}\frac{\partial}{\partial \xi^i}[J U^i]=0, \quad J U^i = b^i_\alpha \bar{U}^\alpha. \tag{8}$$

The standard form for the momentum equations is

$$J\frac{\partial \bar{U}^\alpha}{\partial t}+\frac{\partial}{\partial \xi^i}[J U^i \bar{U}^\alpha]+\frac{\partial}{\partial \xi^i}[b^i_\alpha (p+\tfrac{2}{3}k)]=T_\alpha \equiv \frac{\partial}{\partial \xi^i}\left[J(\nu+\nu_{\mathrm{T}})\, g^{ij}\frac{\partial \bar{U}^\alpha}{\partial \xi^j}\right]+\frac{\partial}{\partial \xi^i}\left[J^{-1}\nu_{\mathrm{T}}\, b^i_\beta\, b^m_\alpha \frac{\partial \bar{U}^\beta}{\partial \xi^m}\right]. \tag{9}$$

The following master equation, which will be used later, results easily from (9):

$$J\frac{\partial \bar{U}^\alpha}{\partial t}+\frac{\partial f^i_\alpha}{\partial \xi^i}=0,$$

where

$$f^i_\alpha = J U^i \bar{U}^\alpha - J(\nu+\nu_{\mathrm{T}})\, g^{ij}\left.\frac{\partial \bar{U}^\alpha}{\partial \xi^j}\right|_{j=i} - s^i_\alpha + b^i_\alpha (p+\tfrac{2}{3}k), \tag{10}$$

and

$$s^i_\alpha = \left[J(\nu+\nu_{\mathrm{T}})\, g^{ij}\frac{\partial \bar{U}^\alpha}{\partial \xi^j}\right]_{j\neq i} + J^{-1}\nu_{\mathrm{T}}\, b^i_\beta\, b^m_\alpha \frac{\partial \bar{U}^\beta}{\partial \xi^m}. \tag{11}$$

s^i_α vanishes if the grid is orthogonal (then $g^{ij}=0$ for $i\neq j$) and if the flow is laminar ($\nu_{\mathrm{T}}=0$).

3. THE NUMERICS

3.1. *Introduction*

In order to build numerical schemes in which pressure and velocity share the same location without introducing the classical odd-even decoupling problem for the pressure field, we consider the following one-dimensional model:

$$\frac{\mathrm{d}F}{\mathrm{d}x}=0, \qquad F(x)=a(x)\frac{\mathrm{d}\mathscr{U}}{\mathrm{d}x}-b(x)\,\mathscr{U}-\mathscr{P}(x) \tag{12}$$

which describes the conservation of the 'flux' $F(x)$ for the 'momentum' unknown $\mathscr{U}(x)$. The source term $\mathscr{P}(x)$ is included to simulate the pressure gradient term. We consider the cell $[0, h]$ over which a and b are assumed constant while $\mathscr{P}(x)$ is supposed to be piecewise constant:

$$\mathscr{P}(x)=P_{1/2}, \tag{13a}$$

or to vary linearly:

$$\mathscr{P}(x)=P_0+\sigma x, \quad \sigma=h^{-1}(P_1-P_0). \tag{13b}$$

Using the boundary condition $\mathscr{U}(0)=U_0$, two successive quadratures of (12) yield the following 'shape function':

$$\mathscr{U}(x)=U_0 \mathrm{e}^{Rx}-\frac{1}{b}\left[\sigma\left(x+\frac{1-\mathrm{e}^{Rx}}{R}\right)+(P_0+\bar{F})(1-\mathrm{e}^{Rx})\right], \tag{14}$$

where $R=b/a$. The value of the flux $\bar{F}$ then results from the boundary condition $\mathcal{U}(h)=U_1$:

$$\bar{F}=\frac{b}{e^{\gamma}-1}U_1-\frac{be^{\gamma}}{e^{\gamma}-1}U_0-(P_1-P_0)\left[\frac{e^{\gamma}-\gamma-1}{\gamma(e^{\gamma}-1)}\right]-P_0, \tag{15}$$

where $\gamma\equiv Rh$ is the cell Reynolds number. In equations (14) and (15), the particular case (13a) results from the substitution (S): $\sigma=0$; $P_0\rightarrow P_{1/2}$.

The 'shape function' (14) for $\mathcal{U}(x)$ is used to get the midpoint value $U_{1/2}$; this defines the so-called reconstruction step

$$U_{1/2}\equiv\mathcal{U}\left(\frac{h}{2}\right)=\lambda e^{\gamma/2}U_0+\lambda U_1-K(P_1-P_0), \tag{16}$$

where

$$\lambda\equiv\frac{1}{e^{\gamma/2}+1}\quad\text{and}\quad K\equiv\frac{\tanh(\gamma/4)}{2b}.$$

By contrast to the standard interpolation practice: $U_{1/2}=(U_0+U_1)/2$, the important characteristic of this equation is that, for $\sigma\neq0$, $U_{1/2}$ is related not only to U_0 and U_1, but also to the nodal pressures P_0 and P_1 on both sides of point 1/2. Because these pressure values directly influence $U_{1/2}$, this feature provides the coupling between pressure and velocity necessary to circumvent chequerboard oscillations. Equation (16) shows also that only the linearized part of the source term contributes to the reconstructed midvalue—the local constant P_0 in (14) disappears when (15) is substituted in (14)—and, with the substitution (S), the reconstruction (16) no longer depends on the local pressure gradient.

It is instructive to examine the dependence of $U_{1/2}$, as determined by (16), for limiting values of the mesh Reynolds number: it is found that

$$\text{if } \gamma\rightarrow0^{\pm},\qquad \text{then } U_{1/2}\rightarrow\tfrac{1}{2}(U_0+U_1)-\frac{h}{8a}(P_1-P_0), \tag{17a}$$

$$\text{if } \gamma\rightarrow\infty,\qquad \text{then } U_{1/2}\rightarrow U_0-\frac{1}{2b}(P_1-P_0), \tag{17b}$$

$$\text{if } \gamma\rightarrow-\infty,\qquad \text{then } U_{1/2}\rightarrow U_1+\frac{1}{2b}(P_1-P_0), \tag{17c}$$

In both cases, the dependence of the nodal velocities U_0 and U_1 moves from equal influence of U_0 and U_1 at $\gamma=0$ toward a fully upwind influence as $|\gamma|\rightarrow\infty$, this effect being independent of (13a) or (13b). Also, the pressure gradient (source term) balances the dominant term in the equation, for $\sigma\neq0$, and allows a more physical reconstruction. The asymptotic forms (17) are identical to those obtained in Reference 16. However, in contrast with that of Reference 16, the shape function (14) and the reconstructed midpoint value (16) are here exact solutions of the linear problem.

It is now easy to obtain the one-dimensional scheme to be used when the flux balance is written over two adjacent cells DC and CU, according to Figure 1(a):

$$0=\int_{u}^{d}\frac{dF}{dx}\,dx=F_d-F_u, \tag{18}$$

where F_d and F_u are identified with $\bar{F}_d$ and $\bar{F}_u$, respectively, and evaluated from (15). Equation (18) allows the resulting scheme (19) to be obtained:

$$C_C U_C+C_D U_D+C_U U_U=\Gamma_d(P_D-P_C)+\Gamma_u(P_C-P_U), \tag{19}$$

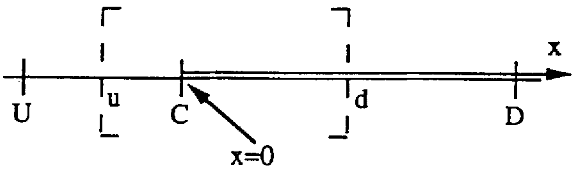

Figure 1(a). One-dimensional model. Control volume; location of grid points U, C, D and of fluxes u, d

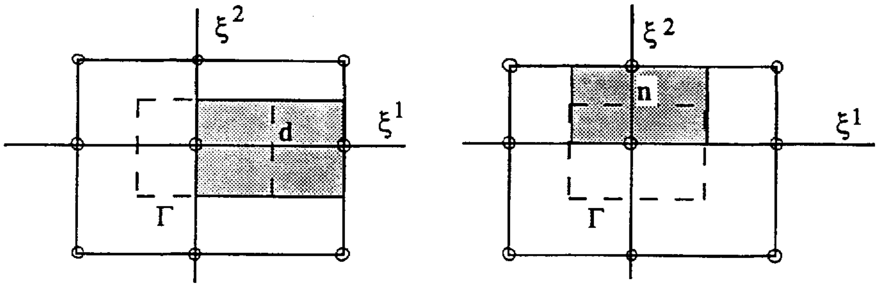

Figure 1(b). Two-dimensional example for the (shadowed) staggered volumes V_1 (surrounding d) and V_2 (surrounding n) used to estimate fluxes at d and n, respectively. O, grid points and location of unknowns.----, boundaries of the control volume

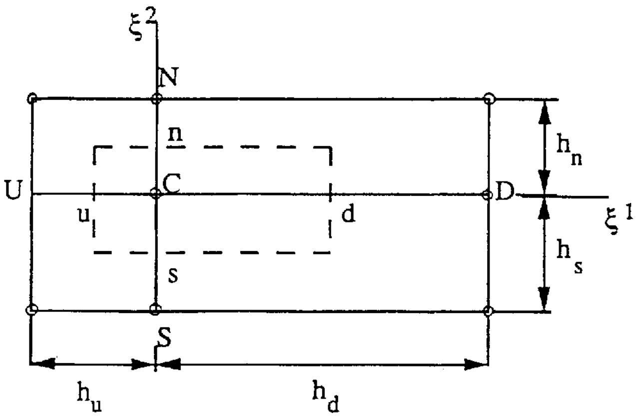

Figure 1(c). Two-dimensional example for the control volume. O, grid points and location of unknowns.----, boundaries of the control volume

where the influence coefficients are

$$C_D = b_d\varphi_d, \qquad C_U = b_u(1+\varphi_u), \qquad C_C = -[C_D + C_U] - [b_d - b_u] \equiv -[b_d(1+\varphi_d) + b_u\varphi_u],$$

$$\Gamma_d = \frac{1}{\gamma_d} - \varphi_d, \qquad \Gamma_u = -\frac{1}{\gamma_u} + 1 + \varphi_u, \tag{20}$$

where $\varphi \equiv 1/(e^{\gamma-1})$.

The truncation error of (19) and (20) defined by

$$\tau(x_{\mathrm{C}})=h^{-1}[C_{\mathrm{C}}\mathscr{U}_{\mathrm{C}}+C_{\mathrm{D}}\mathscr{U}_{\mathrm{D}}+C_{\mathrm{U}}\mathscr{U}_{\mathrm{U}}-\Gamma_{\mathrm{d}}(\mathscr{P}_{\mathrm{D}}-\mathscr{P}_{\mathrm{C}})-\Gamma_{\mathrm{u}}(\mathscr{P}_{\mathrm{C}}-\mathscr{P}_{\mathrm{U}})]$$

can be written as

$$\tau(x_{\mathrm{C}})=\frac{h}{24}\left[\kappa^2-1)\Phi(x_{\mathrm{C}})+\frac{h}{2}(\kappa^2+1)\frac{\mathrm{d}\Phi}{\mathrm{d}x}(x_{\mathrm{C}})\right]+O(h^3) \tag{21a}$$

with

$$\Phi(x)=a\frac{\mathrm{d}^3\mathscr{U}}{\mathrm{d}x^3}-3\left[\frac{\mathrm{d}^2\mathscr{P}}{\mathrm{d}x^2}+b\frac{\mathrm{d}^2\mathscr{U}}{\mathrm{d}x^2}\right]+2R\left[\frac{\mathrm{d}\mathscr{P}}{\mathrm{d}x}+b\frac{\mathrm{d}\mathscr{U}}{\mathrm{d}x}\right]. \tag{21b}$$

Since $h\equiv h_{\mathrm{u}}=h_{\mathrm{d}}/\kappa$, the scheme (19) and (20) is formally first-order accurate on stretched grids and second-order accurate on uniform grids. The weighting coefficients C_{D}, C_{U}, C_{C} provide the classical upwinding effect due to advection; the main difference with respect to the classical exponential scheme—produced on the convective form of the equation—is the introduction of the mean divergence term $[\mathrm{d}b/\mathrm{d}x]$ over the cell, namely: $b_{\mathrm{d}}-b_{\mathrm{u}}$. When $\sigma\neq 0$, a new embodied feature arises: the weighting coefficients Γ_{d} and Γ_{u} for the pressure gradients allow a built-in upwinding *of the source term* depending on the value of cell Reynolds numbers γ_{u} and γ_{d}.

However, with (13a), the pressure gradient is frozen to $P_{\mathrm{d}}-P_{\mathrm{u}}$ and no upwinding is present in the source term. Because (16) does not provide a pressure gradient, another reconstruction must supply (16). We first note that (19), still valid with $\Gamma_{\mathrm{d}}=\Gamma_{\mathrm{u}}=1/2$, becomes

$$U_{\mathrm{C}}=\hat{U}_{\mathrm{C}}+K_{\mathrm{C}}[P_{\mathrm{D}}-P_{\mathrm{U}}] \text{ with } \hat{U}_{\mathrm{C}}=-\frac{1}{C_{\mathrm{C}}}[C_{\mathrm{D}}U_{\mathrm{D}}+C_{\mathrm{U}}U_{\mathrm{U}}],\quad K_{\mathrm{C}}=\frac{1}{2C_{\mathrm{C}}}. \tag{22}$$

The Rhie and Chow method,[17] which is used here consists in writing an equation similar to (22) at points d and u, namely:

$$U_{\mathrm{d}}=\hat{U}_{\mathrm{d}}+K_{\mathrm{d}}[P_{\mathrm{D}}-P_{\mathrm{C}}],\qquad U_{\mathrm{u}}=\hat{U}_{\mathrm{u}}+K_{\mathrm{u}}[P_{\mathrm{C}}-P_{\mathrm{U}}]. \tag{23}$$

The $\hat{U}$ field is available at nodes C, D, U; it is reconstructed at d and u according to

$$\hat{U}_{\mathrm{u}}=\tfrac{1}{2}[U_{\mathrm{C}}+U_{\mathrm{U}}],\qquad \hat{U}_{\mathrm{d}}=\tfrac{1}{2}[U_{\mathrm{C}}+U_{\mathrm{D}}],\qquad K_{\mathrm{d}}=\tfrac{1}{2}[K_{\mathrm{C}}+K_{\mathrm{D}}],\qquad K_{\mathrm{u}}=\tfrac{1}{2}[U_{\mathrm{C}}+U_{\mathrm{D}}]. \tag{24}$$

Before closing this section, we consider the treatment of the constraint $\mathrm{d}U/\mathrm{d}x=0$ which mimics the incompressibility condition. The method is similar to that used for F (see (15)) and it makes use of $U_{\mathrm{d}}-U_{\mathrm{u}}=0$. With (16), as well as with (23), a different pressure gradient is substituted into U_{d} and U_{u}, for this reason, the chequerboard oscillation is avoided and the source equation takes the form

$$(K_{\mathrm{d}}+K_{\mathrm{u}})P_{\mathrm{C}}-K_{\mathrm{d}}P_{\mathrm{D}}-K_{\mathrm{u}}P_{\mathrm{U}}=-[\hat{U}_{\mathrm{d}}-\hat{U}_{\mathrm{u}}], \tag{25}$$

where

$$\hat{U}_{\mathrm{d}}=\lambda_{\mathrm{d}}U_{\mathrm{D}}+(1-\lambda_{\mathrm{d}})U_{\mathrm{C}},\qquad \hat{U}_{\mathrm{u}}=(1-\lambda_{\mathrm{u}})U_{\mathrm{U}}+\lambda_{\mathrm{u}}U_{\mathrm{C}}$$

with

$$\lambda=\frac{1}{\mathrm{e}^{\gamma/2}+1}=\frac{1}{2}\left[1-\tanh\frac{\gamma}{4}\right]$$

while

$$K=\frac{\tanh(\gamma/4)}{2b}$$

if $\sigma \neq 0$ and (24) if $\sigma = 0$. This relationship can be interpreted as a discrete solution of the elliptic problem:

$$-\frac{\mathrm{d}}{\mathrm{d}x}\left[K\frac{\mathrm{d}P}{\mathrm{d}x}\right] = -\operatorname{div}\hat{\mathrm{U}}. \tag{26}$$

The discrete solution of (26) is diagonally dominant in pressure; moreover, for $\sigma \neq 0$, the relative influence of nodal pressures in this mass equation diminishes when the mesh Reynolds number increases while div $\hat{\mathrm{U}}$ becomes its upwind representation $U_\mathrm{C} - U_\mathrm{U}$.

3.2. Multidimensional extension

After a fully implicit time-discretization, the linearized momentum master equation (11) becomes

$$J\frac{[\bar{U}^\alpha]^n - [\bar{U}^\alpha]^{n-1}}{\tau} + \frac{\partial F^i_\alpha}{\partial \xi^i} = 0, \tag{27}$$

where F^i_α is the linearized time-discrete form of f^i_α introduced in (11); namely:

$$\begin{aligned} F^i_\alpha \equiv {} & [JU^i]^{n-1}[\bar{U}_\alpha]^n + b^i_\alpha p^n - J[\nu + \nu_\mathrm{T}]^{n-1} g^{ij}\left[\frac{\partial \bar{U}^\alpha}{\partial \xi^j}\right]^n_{j=i} \\ & - J[\nu + \nu_\mathrm{T}]^{n-1} g^{ij}\left[\frac{\partial \bar{U}^\alpha}{\partial \xi^j}\right]^{n-1}_{j\neq i} - J^{-1} b^k_\alpha b^i_\beta\left[\nu_\mathrm{T}\frac{\partial \bar{U}^\beta}{\partial \xi^k}\right]^{n-1} \end{aligned} \tag{28}$$

In the time derivative, the mean value over the control volume is lumped on its node centre. There are five contributions in the momentum flux F^i_α, from the left to the right: the convective term, the 'augmented' pressure term $P = (p + 2k)/3$ and the three transport terms. For each of them, the lagged contributions at previous time step t^{n-1} are indicated. The two last terms of (28) define the time-explicit contribution (11), s^i_α. The closure assumptions are the same as in Section 3.1. It is assumed that $[JU^i]^{n-1}$, $J[\nu + \nu_\mathrm{T}]^{n-1} g^{ij}$ and $J^{-1}\ b^k_\alpha[\nu_\mathrm{T}(\partial \bar{U}^\beta/\partial\xi^k)]^{n-1}$ are approximated by their mean values at the centre of the staggered volume V_i (see Figure 1(b)). This generalizes the assumption that a and b are constant in (12). The term P can be assumed either piecewise constant, as in (12b), or linear in the ξ^i direction, in agreement with (13b). It can be noted that the face area b^i_α is available without approximation due to the geometric conservation property.

The shape function (14) is used over volumes V_i to construct the fluxes $F^1_{\alpha\mathrm{u}}$, $F^1_{\alpha\mathrm{d}}$, $F^2_{\alpha\mathrm{n}}$, $F^2_{\alpha\mathrm{s}}$, $F^3_{\alpha\mathrm{e}}$, $F^3_{\alpha\mathrm{w}}$. The result is of course similar to (15). For instance,

$$F^1_{\alpha\mathrm{d}} = [JU^1]^{n-1}_\mathrm{d}\ \varphi_{1\mathrm{d}}\bar{U}^\alpha_\mathrm{D} - [JU^1]^{n-1}_\mathrm{d}(1 + \varphi_{1\mathrm{d}})\bar{U}^\alpha_\mathrm{C} + \underline{[b^1_\alpha]_\mathrm{d}\left[\frac{1}{\gamma_{1\mathrm{d}}} - \varphi_{1\mathrm{d}}\right][P_\mathrm{D} - P_\mathrm{C}]} - [b^1_\alpha]_\mathrm{d} P_\mathrm{C} - S^1_{\alpha\mathrm{d}}, \tag{29}$$

where $S^1_{\alpha\mathrm{d}}$ is the linearized time-discrete value of s^1_α at point d. With the substitution (S), the underlined term is omitted and P_C in (29) becomes P_d.

The integration of the momentum equation (25) over the control volume around point C (Figure 1(c)) gives (30):

$$J_\mathrm{C}\frac{[\bar{U}^\alpha]^n_\mathrm{C} - [\bar{U}^\alpha]^{n-1}_\mathrm{C}}{\tau} + F^1_{\alpha\mathrm{d}} - F^1_{\alpha\mathrm{u}} + F^2_{\alpha\mathrm{n}} - F^2_{\alpha\mathrm{s}} + F^3_{\alpha\mathrm{e}} - F^3_{\alpha\mathrm{w}} = 0. \tag{30}$$

Substituting expressions like (29) into (30), in the same way as (15) was substituted into (18), yields a seven-point scheme for the velocity and for the pressure.

Now, the continuity equation involves the contravariant velocity component U^i:

$$[JU^1]_\mathrm{d}-[JU^1]_\mathrm{u}+[JU^2]_\mathrm{n}-[JU^2]_\mathrm{s}+[JU^3]_\mathrm{e}-[JU^3]_\mathrm{w}=0. \tag{31}$$

However, the reconstructed components are the Cartesian velocity components $\bar{U}^\alpha$ which are obtained using (16) or the procedure.[17] Equation (16) gives rise to the correction equation:

$$\bar{U}^\alpha_\mathrm{d}=\hat{U}^\alpha_\mathrm{d}-\frac{\tanh \gamma_{1\mathrm{d}}/4}{2[JU^1]^{n-1}}\,b^1_{\alpha\mathrm{d}}\,[P_\mathrm{D}-P_\mathrm{C}], \quad \text{where} \quad \hat{U}^\alpha_\mathrm{d}=\lambda_\mathrm{d}\,\bar{U}^\alpha_\mathrm{D}+(1-\lambda_\mathrm{d})\,\bar{U}^\alpha_\mathrm{C}. \tag{32}$$

Equation (32) involves the pressure gradient in the ξ^α direction only, because of the one-dimensional character of the reconstruction. This is why the procedure[17] is preferred since it involves the full pressure gradient $\partial P/\partial \bar{x}^\alpha$ in $\bar{U}^\alpha$ instead of only $\partial P/\partial \xi^\alpha$, as in (32). The needed contravariant velocity components, in (30), result from the Cartesian velocity components through

$$JU^i=b^i_\alpha\,\bar{U}^\alpha \quad \text{at points d, u, n, s, e, w.} \tag{33}$$

3.3. The pressure–velocity coupling problem

The pressure–velocity coupling is handled with the so-called PISO procedure.[18]

Step 1. In the cell-centred collocated grid approach, where velocity components, pressure and turbulent quantities are defined at the centre of the control volume, the momentum equations (31) can be written in the form (34) for the Cartesian velocity component $\bar{U}^\alpha$, $\alpha=1$ (here and in the following, other components $\alpha=2$, 3 which take a similar form, are omitted).

$$\left[\frac{J_\mathrm{C}}{\tau}+C_\mathrm{C}\right]\bar{U}^1_\mathrm{C}=\sum_1^6 C_\mathrm{nb}\,\bar{U}^1_\mathrm{nb}+\frac{J_\mathrm{C}}{\tau}\,[\bar{U}^1]^{n-1}_\mathrm{C}-\left[b^i_1\,\frac{\partial P}{\partial x^i}+\frac{\partial S^i_1}{\partial \xi^i}\right]_\mathrm{C}. \tag{34}$$

In (34), as in the following, the index n has also been omitted so that $\bar{U}^1$ is the predicted Cartesian (non-solenoidal) velocity component at time t^n. The coefficients $C_\mathrm{C}+J_\mathrm{C}/\tau$ are computed at the cell centre, according to

$$C_\mathrm{C}=-\{(JU^1)^{n-1}_\mathrm{d}\,[1+\varphi_{1\mathrm{d}}]+(JU^1)^{n-1}_\mathrm{u}\,\varphi_{1\mathrm{u}}\}.$$

As indicated in the nomenclature, the summation over nb involves the velocity unknowns $\bar{U}^1$ at the six nodal points U, D, N, S, E, W. The pressure contribution in (34) is known from the previous iteration. Equations like (34) provide the predicted velocity components $\bar{U}^\alpha$ at grid points C, U, D, . . . from the given velocity $\mathbf{U}^{n-1}$ and pressure fields.

Step 2. It defines the velocity $\hat{\mathbf{U}}$ before projection. Following the step which led from (19) to (22), equations like (34) can be recast under the form

$$\bar{U}^1_\mathrm{C}=\hat{\bar{U}}^1_\mathrm{c}-\left[\frac{J_\mathrm{C}}{\tau}+C_\mathrm{C}\right]^{-1}\left[b^j_1\,\frac{\partial P}{\partial \xi^j}\right]_\mathrm{C}. \tag{35}$$

Using (24), equations like (35) provide the Cartesian co-ordinates $\hat{\bar{U}}^1_\mathrm{d}$, $\hat{\bar{U}}^1_\mathrm{n}$, . . . of the field $\hat{\mathbf{U}}$ on the faces d, u, n, s, e, w of the mass control volume. By means of (32), we obtain the reconstructed fluxes $J\hat{U}^i$. Hence, the projection equation can be written at each point d, u, n, s, e, w:

$$[JU^i]_\mathrm{d}=[J\hat{U}^i]_\mathrm{d}-K_\mathrm{d}\,[g^{ij}]_\mathrm{d}\left[\frac{\partial P}{\partial \xi^j}\right]_\mathrm{d}, \tag{36}$$

where K_d is given, as in (24), by the reconstruction,[17] namely:

$$K_\mathrm{d}=\tfrac{1}{2}\,[K_\mathrm{C}+K_\mathrm{D}]=\frac{1}{2}\left[\left(\frac{J_\mathrm{C}}{\tau}+C_\mathrm{C}\right)^{-1}+\left(\frac{J_\mathrm{D}}{\tau}+C_\mathrm{D}\right)^{-1}\right].$$

The K_d coefficient then appears as independent of the corresponding velocity component, i.e. on α in (32). This is because the same advection–diffusion operator applies to the three $\bar{U}^\alpha$ equations see (9)). The g^{ij} terms, $i \neq j$, in (36) are generated by the misalignment between the co-ordinate lines and the directions of the velocity components. Now, in (36), the fluxes JU^i at the faces and the pressure field P at the grid points are not known yet. This equation is to be used now only to establish the equation for P.

Step 3. Substituting (36) into the continuity equation (30) yields the pressure field which generalizes (26) and can be viewed as the solution of the continuous equation (37):

$$-\frac{\partial}{\partial \xi^i}\left[JK\,Jg^{ij}\frac{\partial P}{\partial \xi^j}\right] = -\frac{\partial[J\hat{U}^i]}{\partial \xi^i}. \tag{37}$$

The products JK and Jg^{ij} are evaluated at midpoints d, u for $i=j=1$, n, s for $i=j=2$, e, w for $i=j=3$. Among the whole set of contributions to the pressure matrix, it is necessary to keep all the fluxes in order to allow a complete construction of the coefficients, $i=j$, because of the misalignment problem. Only the seven nodes: U, D, N, S, E, W, P, which come from second-order derivatives $\partial^2/\partial\xi^i\partial\xi^j$, $i=j$ are, thus, treated implicitly. Extradiagonal coefficients $i \neq j$ arising from crossed second-order derivatives $\partial^2/\partial\xi^i\partial\xi^j$ are connected to the level of non-orthogonality of the grid. They are not retained implicitly but rather treated as source terms. As a result, diagonal dominance and symmetry of the discretized pressure matrix are easily obtained. The method used to reconstruct non-available Cartesian velocity components as well as the pressure solver to get the solution of (37) are the same as in Reference 19 and are not detailed here. Let us only mention that the discrete pressure solution of (37) is obtained by means of an incomplete LU-preconditioned conjugate gradient method.

Step 4. The correction procedure uses the pressure field resulting from Step 3 to compute the divergence free velocity field. This projection step is written for the Cartesian velocity components rather than for the fluxes. Hence, equations like (35), which are used instead of (36), provide the updated velocity field $\mathbf{V}^n$.

4. RESULTS

Conventional boundary layer calculations[6–8] that have been carried out break down over more than one-third of the viscous zone. They are sometimes limited in the leeside plane of symmetry (up to $x/L \approx 0{\cdot}4$ in Reference 7, to $x/L \approx 0{\cdot}9$ in Reference 8) and cover always only the windward part, for an angle $\theta < \theta_s$. Values of θ_s depend on the numerical methods: $\theta_s \approx 110°$ in Reference 7, θ_s is a linear function of x/L in Reference 8 with $\theta_s \approx 150°$ for $x/L = 0{\cdot}15$ and $\theta_s \approx 120°$ for $x/L = 0{\cdot}9$ using the potential pressure distribution, while $\theta_s \approx 120°$ with the experimental pressure distribution. For Navier–Stokes type calculations, apart from Reference 9, where comparisons are qualitative and limited to surface data (their Figures 14 to 16), the only informative contribution is Reference 10. While Reference 11 addresses the case $Re = 7{\cdot}7 \times 10^6$, the results that are now presented focus, like References 6–10, on the case $Re = 7{\cdot}2 \times 10^6$. A C–O-type grid is used with a 'sinh' stretching in the normal direction ξ^2. The normalized spacing, along ξ^2, is less than 10^{-5} near the wall in order to resolve the thin viscous zones, present in high Reynolds number flows, down to the viscous sublayer. In order to indicate how results depend on the grid, calculations have been performed on a coarse grid (Plate 1) consisting of $70(\xi^1) * 41(\xi^2) * 41(\xi^3)$ points as well as on a fine grid with $120(\xi^1) * 60(\xi^2) * 60(\xi^3)$ points, where ξ^1 is in the axial direction and ξ^3 is along the girth. In all cases, the laminar calculations have been continued up to the experimentally observed transition line along which the turbulence model is activated. The fine grid results have been obtained after a series of successive runs, each taking 2700 s on Cray 2. In the first run, the flow is laminar and 42 global iterations are performed, starting from uniform flow conditions. Then, the model[13] is switched on and three runs allow to perform 92, 114, 114 iterations. Finally, 82 iterations are performed with the corrections[14] introduced. The flow is considered to be fully converged before the corrections[14] are switched on: all the equation residuals have decreased everywhere by more than three orders of magnitude. After the switch of corrections,[14] the residuals decrease again and ultimately oscillate at levels similar to those obtained before the switch. Therefore, the CPU effort on Cray 2, per grid point and per fine grid iteration, varies between 15×10^{-5} and $5{\cdot}48\times10^{-5}$ s, with an average of 7×10^{-5} s, for a storage of 30 double precision Mwords. The radial sinh clustering is similar for both grids. In the girthwise direction, a sinh clustering makes resolution $\Delta\theta$ decrease continuously from $\theta=0°$, where $\Delta\theta\approx4°$ to $\theta=180°$, where $\Delta\theta\approx2°$.

The pressure coefficient in the symmetry plane is compared with experiments and with the potential flow solution in Figure 2. The agreement between data and the fine grid results is good on the windward side, at least for $x/L<0{\cdot}8$, and the grid effect is low. In contrast, on the leeside, where the difference between potential flow and experiments indicates a high level of viscous–inviscid interaction, a very strong grid dependency is apparent as well as important discrepancies between predictions and data[20] which start for low values of x/L. The discrepancy between viscous flow calculations and experimental data is very reminiscent of that found in Reference 21. Although the scales plotted in Reference 10 do not allow an accurate comparison,

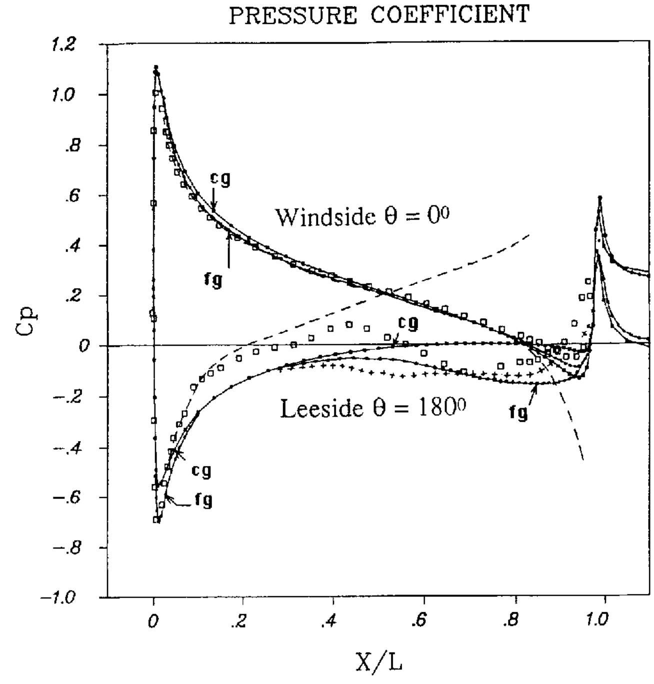

Figure 2. Longitudinal distribution of the pressure coefficient C_p in the vertical plane of symmetry; $Re=7{\cdot}2\times10^6$; incidence 30°. ☐, experimental data[25] (taken from Reference 20); ·—, present computations with a Baldwin–Lomax model with modifications[14] (the dots indicate the location of grid points); cg, coarse grid computation: $70(\xi)\times40(\eta)\times40(\zeta)$; fg, fine grid computation: $120(\xi)\times60(\eta)\times60(\zeta)$. ----, potential flow distribution past the bare spheroid (taken from Reference 20). + + + + +, computations[9] with CFL3D.

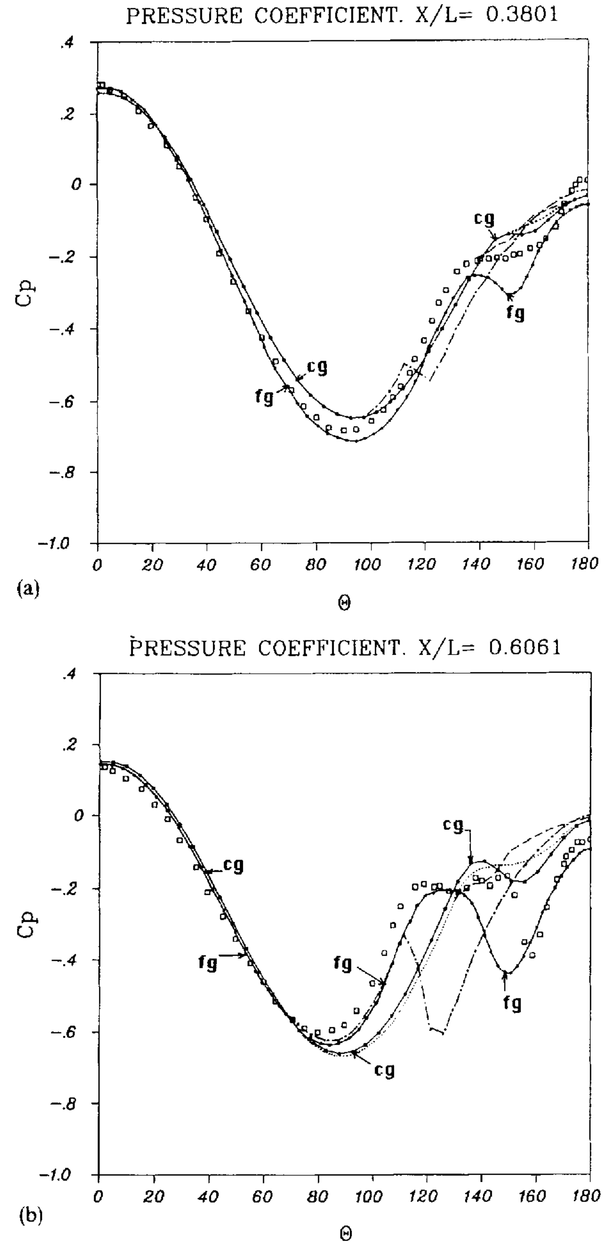

Figure 3. Girthwise distributions of the pressure coefficient C_p for several x/L stations: (a) $x/L=0{\cdot}3801$; (b) $x/L=0{\cdot}6061$; (c) $x/L=0{\cdot}7725$, (d) $x/L=0{\cdot}9167$. $Re=7{\cdot}2\times10^6$; incidence 30°. □, C_p experimental data[4] (taken from Reference 22). ——, present RANSE computations (the dots indicate the location of grid points); Baldwin–Lomax model with modifications;[14] cg, coarse grid computation: $70(\xi)\times40(\eta)\times40(\zeta)$; fg, fine grid computation: $120(\xi)\times60(\eta)\times60(\zeta)$. ...., present RANSE coarse grid computations; Baldwin–Lomax model without modifications.[14] ------, present RANSE coarse grid computations; tanh model (3). —·—, present laminar flow coarse grid computations. – –, potential flow calculations. ◆, TLNS computations[10] with CFL3D. X, TLNS computations[10] with VOR3DI

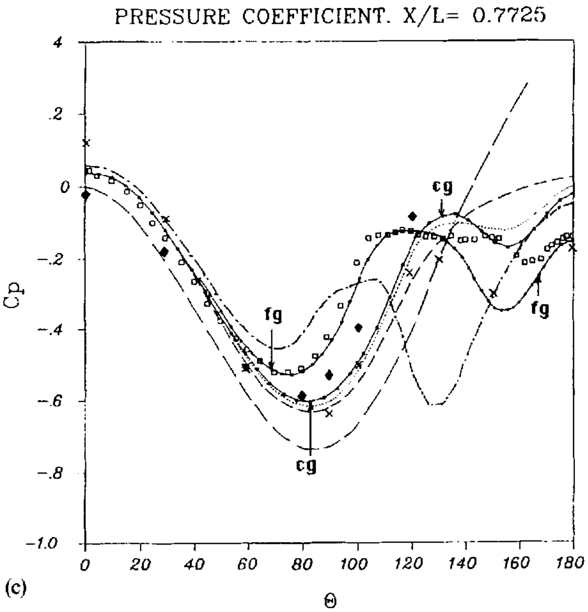

(c)

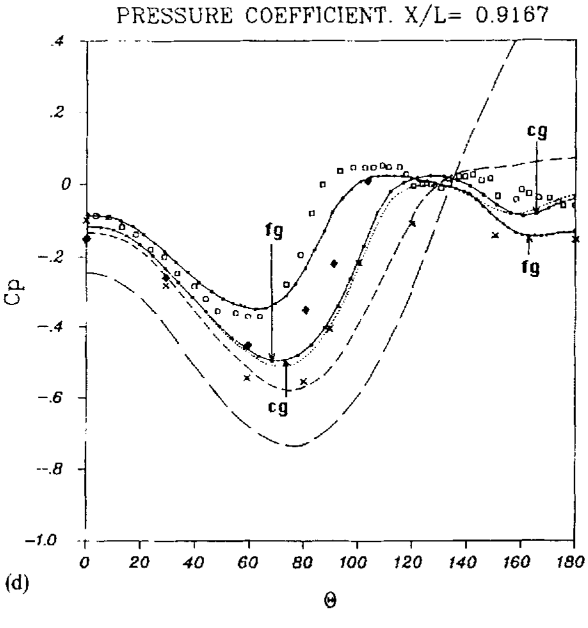

(d)

Figure 3. (Continued)

VOR3DI gives a poor prediction, while present fine grid results and CFL3D results are the best for $x/L<0{\cdot}7$ and $x/L>0{\cdot}7$, respectively. Reasons for the shift with respect to experimental data are not clear. It may be observed that the discrepancy starts very early, about $x/L=0{\cdot}05$ (19 x/L stations are clustered between 0 and 0·055) and that the flow remains laminar for $x/L<0{\cdot}1$, where the shift is already established. The discrepancy with data should, therefore, not be attributed to deficiencies in the turbulence modelling. It will be shown that the area $x/L < 0{\cdot}2$ is critical for the global flow behaviour; the reason being that transition occurs there, this probably causes the difference between computations and data.

Girthwise pressure distributions are compared in Figure 3 for several values of x/L. Presented results show strong discrepancies between laminar flow and turbulent flow calculations. The level of global improvement provided by the modifications[14] of the model[13] is rather low on the coarse grid and predictions of the 'tanh' model (3)—which gives results identical to those of the Cebeci–Smith model—are worse than those of Baldwin and Lomax. This seems to indicate that, in spite of its lack of frame indifference, the vorticity is a better sensor for the turbulent eddy viscosity than the second invariant of the mean rate of strain tensor. On the windward side, the level of agreement between the present method and the experimental data is correct. The girthwise pressure gradients are well predicted independently of the tested turbulence models, while, although weak, the grid effect cannot be neglected. Results of CFL3D and VOR3DI appear also poorer. For higher values of θ, the experimental data which are modelled vary with x/L. At midbody ($x/L = 0{\cdot}4812$) the laminar boundary layer becomes transitional at about $\theta \approx 60°$ and fully turbulent for $\theta > 70°$. The level of viscous–inviscid interaction is now particularly high, for $80° < \theta < 120°$, and the quality of predictions strongly depends on the grid. The best results in the girthwise compression region, around $\theta = 120°$, are the present fine grid ones. In spite of the well known inability of presently used turbulent models to predict the details of massive separation, their choice is not very important here. Around $\theta = 130°$, there is a local C_p maximum associated with a minimum of skin friction and with separation (see e.g. Reference 1). The capture of this phenomenon depends on the quality of the grid but also on the correction[22] whose effectiveness increases on finer grids. The C_p maximum is also captured with CFL3D which uses a 75 × 49 × 49 grid with $\Delta\theta = 2°$ for $150° < \theta < 180°$, equivalent to the present method. In contrast, present coarse grid results, where $\Delta\theta = 4{\cdot}5°$, completely miss the phenomenon. More leewards, the local pressure peak is also captured by CFL3D and present fine grid calculations, CFL3D results being generally shifted leewards with respect to the present ones. More downstream, the local pressure peak around $\theta = 160°$ weakens at $x/L = 0{\cdot}725$ and it has disappeared at $x/L = 0{\cdot}92$; a plateau of almost constant pressure for $\theta > 100°$ results ($\partial P/\partial\theta$ is slightly negative at $x/L = 0{\cdot}9167$). The outputs of the present fine grid calculations tend to look better than those of CFL3D, while VOR3DI gives everywhere too negative C_p values. However, both results share in common the fact that the peak is not completely forgotten for $x/L > 0{\cdot}9$. The reason for it might be the lack of fading memory mechanisms in the correction.[14]

Wall shear stress data are presented in Figures 4 and 5. Figure 4 presents comparisons with experimental data in the symmetry planes. While the agreement on the wind side is good, there is a discrepancy on the leeside turbulent region, consistent with the pressure differences noted in Figure 2. Results given by CFL3D and VOR3DI are also indicated; the level of disagreement with experimental data is important in view of their pressure results.

Reasons are made clear in Figure 6 where girthwise shear stress distributions are considered. On the windward side, where the flow is laminar and the shear stress is low, the agreement with the experimental data is correct. Strong discrepancies with experimental data exhibited by CFL3D are due to an incorrect location of the switch to the turbulence model, while VOR3DI is computed as fully turbulent. The strong increase of shear in present calculations is, of course, due to transition (the 'stair' behaviour at $x/L = 0{\cdot}48$, $60° < \theta < 80°$ is due to linear interpolations between the neighbouring computed laminar upstream station and the fully turbulent downstream station). The strong decrease of friction from $\theta = 70°$ to $\theta \approx 130$–$140°$ is associated with the strong pressure variation which drastically influences the accuracy of friction predictions. Thin boundary layer calculations[8] (TBL) performed with the experimental pressure distribution

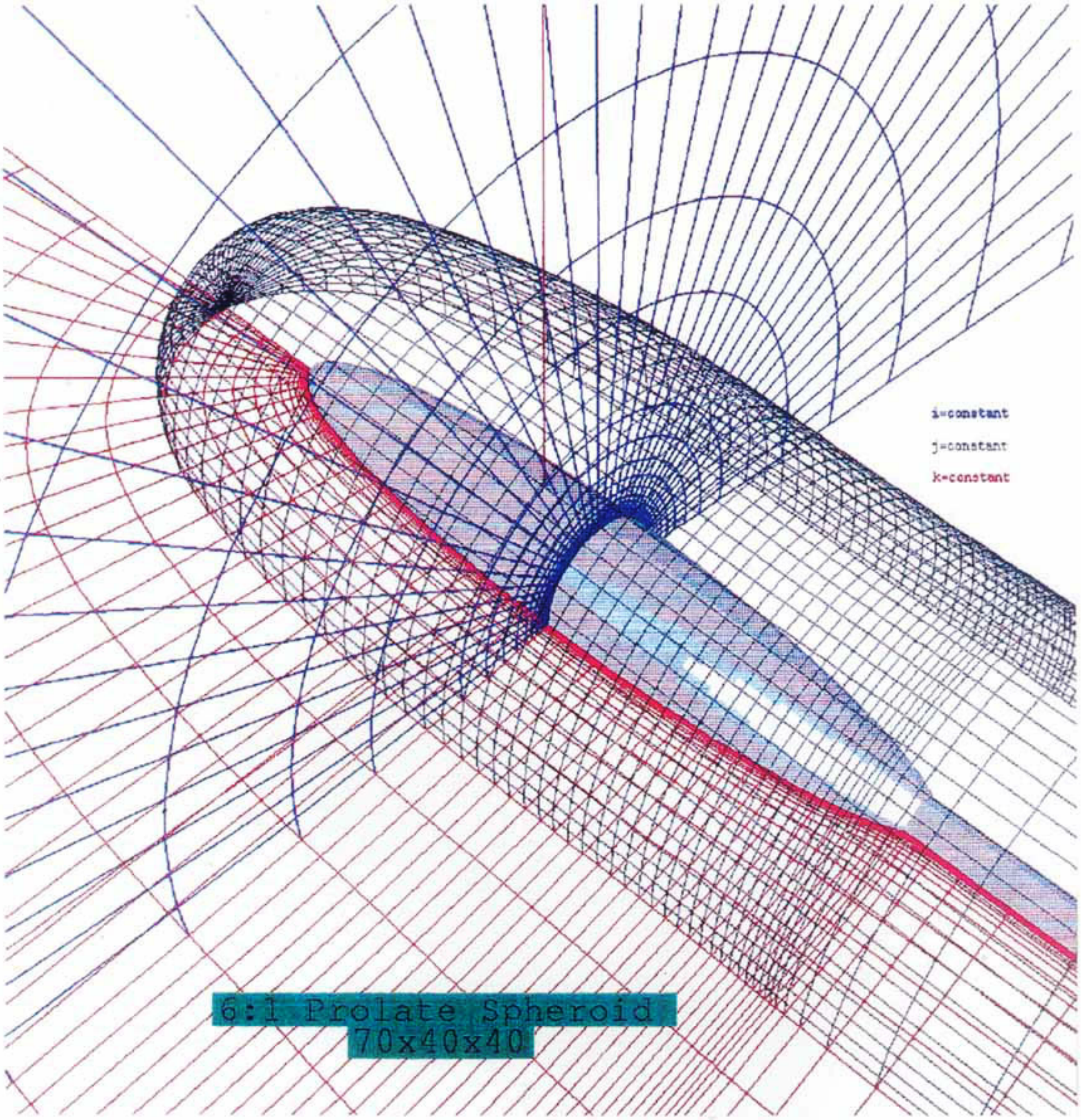

Plate I. 70(ξ)x40(η)x40(ζ) C-O type grid around the 6:1 prolate spheroid

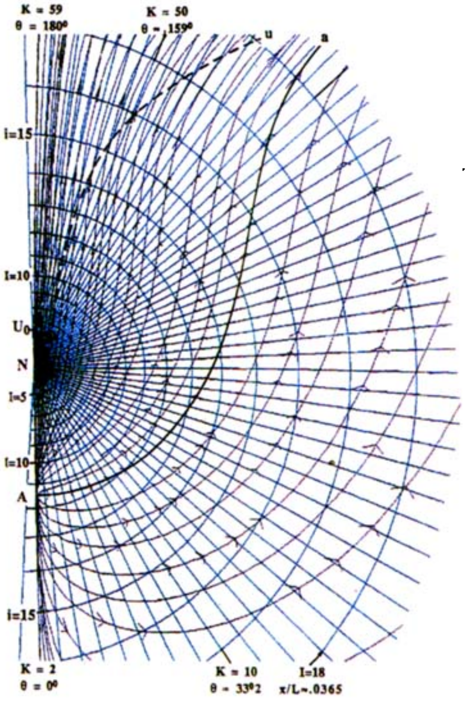

Plate 2(a). Magnified view of computed skin friction lines over a fine grid, 120(ξ)x60(η)x60(ζ), in the forward nose region; grid in green. View from inside the spheroid. ***Re* = 7·2x10^{6}; incidence 30°**. Baldwin–Lomax model with modifications.[14] —— line Aa emanating from the attachment node. —— wall streamlines. ----- GSFmin line

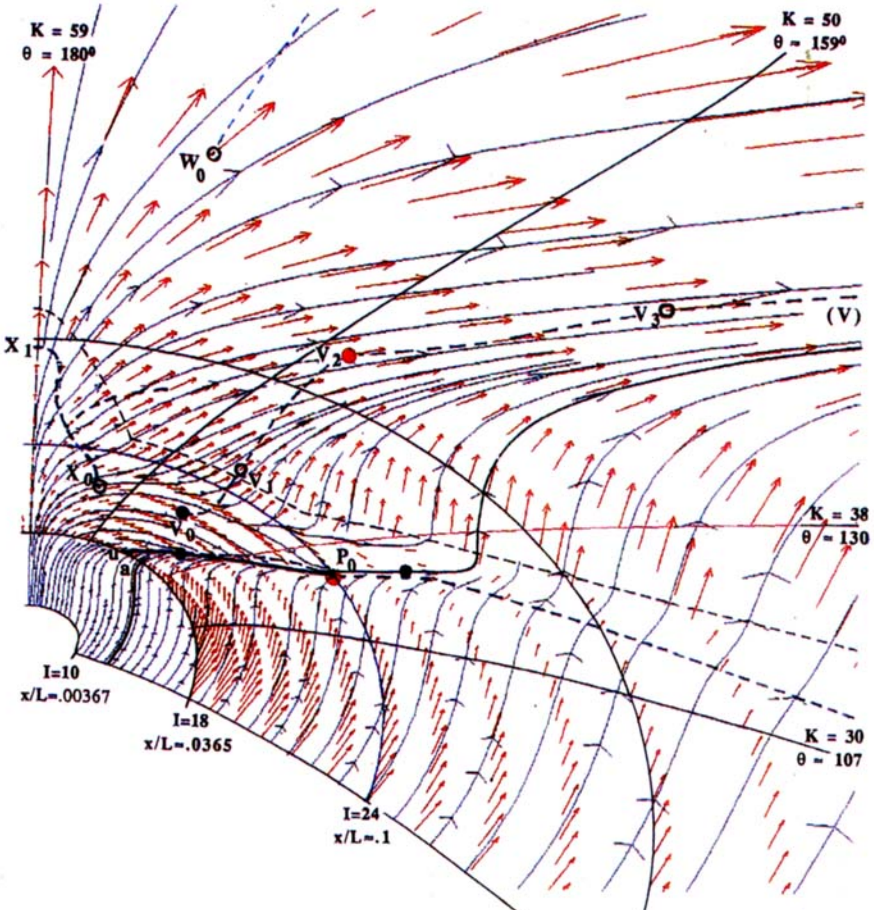

Plate 2(b). View of the wall flow over the forward part of the prolate spheroid. Fine grid 120(ξ)x60(η)x60(ζ). ***Re* = 7·2x10^{6}; incidence 30°**. Baldwin–Lomax model with modifications.[14] ----- grid lines (in black, pink or blue) or skin friction lines (in black). —— particular skin friction line Aa issued from the node A or laminar local separation line passing through P_0. - - - - in green, GSFmin line. - - - - in black, transition line (the flow is laminar on the left of this line, turbulent on the right). → in red, skin friction vectors at grid nodes. Θ, starting point of GSFmin lines. O, points where $|C_f|$ is a local maximum (a pass) over the GSFmin line. ● in red, local minimum of skin friction. ● in black, minimum skin friction, experimental data[1] $x/L \approx 0{\cdot}054$; $\theta \approx 135°8$; $x/L \approx 0{\cdot}138$; $\theta \approx 124°$

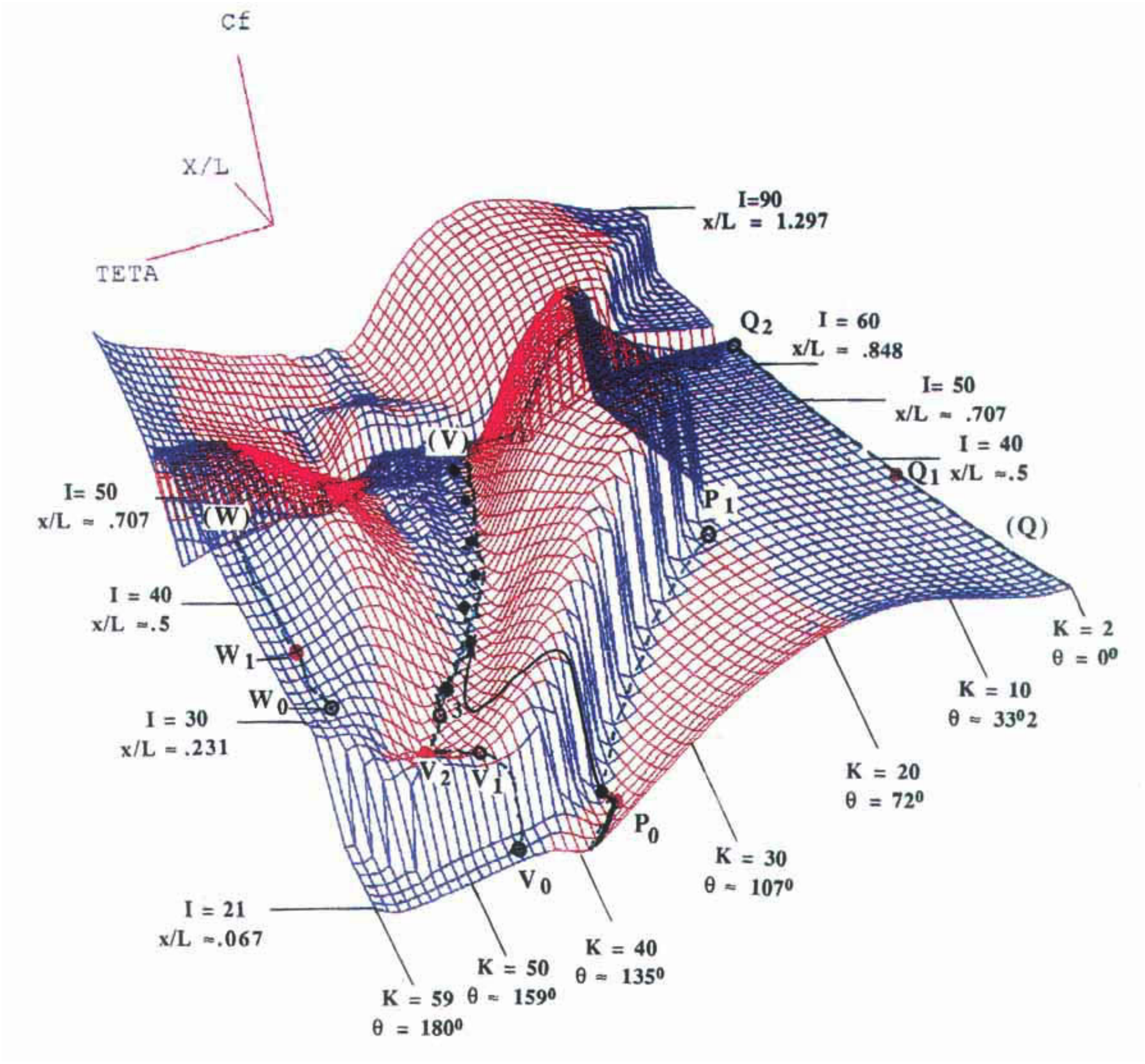

Plate 2(c). Wall shear stress surface coloured by the normal velocity **V·N** at point $\eta = 2$ (the wall is $\eta = 1$). In blue, **V·N** < 0. In red, **V·N** > 0. Fine grid, $120(\xi)\mathrm{x}60(\eta)\mathrm{x}60(\zeta)$. ***Re* = 7·2x10⁶; incidence 30°**. Baldwin–Lomax model with modifications.[14] _ _ _ _ in green, GSFmin line. _____ laminar local separation line starting from P_0 and converging towards the turbulent local separation line (V) starting from V_2. Θ, starting point of GSFmin lines. O, points where $|C_f|$ is a local maximum over the GSFmin line. ● in red, local minimum of skin friction. ●, minimum skin friction, experimental data : $x/L \approx 0{\cdot}138$, $\theta \approx 124°$; $x/L \approx 0{\cdot}306$, $\theta \approx 145°6$; $x/L \approx 0{\cdot}38$, $\theta \approx 133°$; $x/L \approx 0{\cdot}461$, $\theta \approx 128°$; $x/L \approx 0{\cdot}538$, $\theta \approx 121°5$; $x/L \approx 0{\cdot}649$, $\theta \approx 115°2$; $x/L \approx 0{\cdot}725$, $\theta \approx 110°5$; $x/L \approx 0{\cdot}816$, $\theta \approx 105°5$

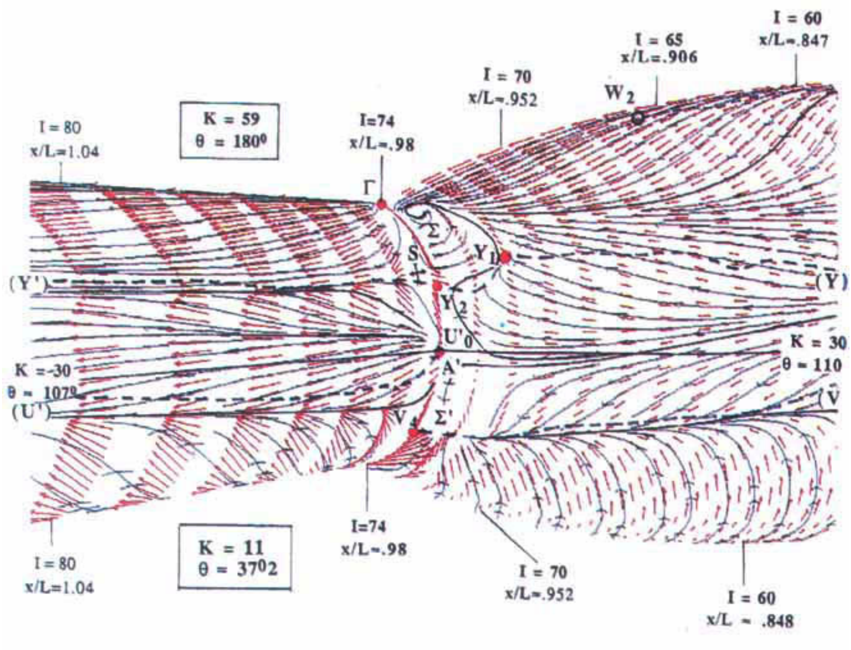

Plate 2(d). Magnified view of the junction region (flow from the right). Fine grid, 120(ξ)x60(η)x60(ζ). ***Re* = 7·2x10⁶; incidence 30°**. Baldwin–Lomax model with modifications.[14] ——— grid line $K = 30$ or skin friction lines (in black). _ _ _ _ in green, GSFmin line. • in red, skin friction vectors at grid nodes. Θ, starting point of GSFmin lines. O, semi pass terminating a GSFmin line. ● in red, local minimum of skin friction

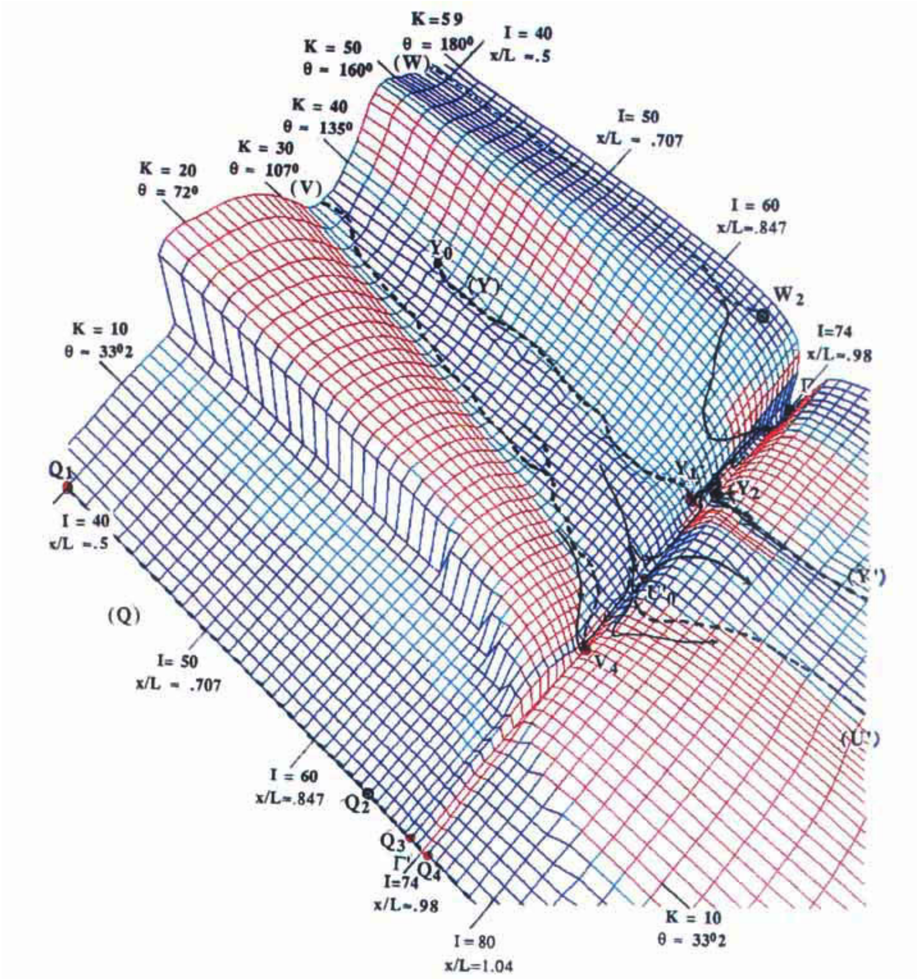

Plate 2(e). Wall shear stress surface coloured by the normal velocity **V·N** at point $\eta = 2$ (the wall is $\eta = 1$). In blue, **V·N** < 0. In red **V·N** > 0. In green, | **V·N** | < 10^{-5}. Fine grid 120(ξ)x60(η)x60(ζ). ***Re* = 7·2x10⁶; incidence 30°**. Baldwin–Lomax model with modifications.[14] _ _ . . _ in green, GSFmin line. ——— some wall streamlines. ●, starting point of GSFmin line (*Y*). O, passes or semi passes. ● in red, local minimum of skin friction

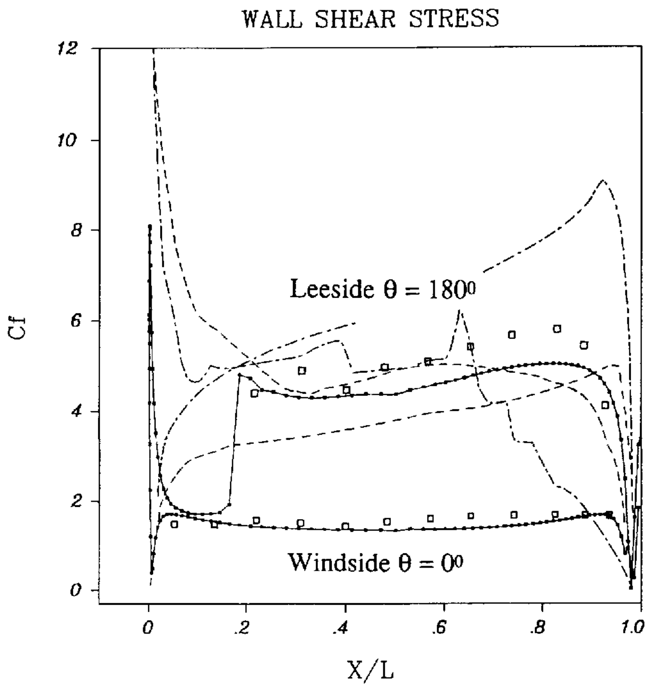

Figure 4. Longitudinal distribution of the skin friction coefficient C_f in the vertical plane of symmetry; $Re = 7{\cdot}2 \times 10^6$; incidence 30°. □, experimental data (taken from Reference 20); , present fine grid computations: $120(\xi) \times 60(\eta) \times 60(\zeta)$ with a Baldwin–Lomax model with modifications[14] (the dots indicate the location of grid points). — — —, TLNS computations[10] with CFL3D. -·—, TLNS computations [10] with VOR3DI

confirm that the pressure variations are the leading phenomenon for this area. They show the excellent computed levels of shear stresses at $x/L = 0{\cdot}48$, $\theta \leqslant 120°$ before the separation-induced breakdown which occurs close to $\theta = 130°$. In this respect, the mentioned better pressure performance of CFL3D and of present fine grid results for $90° < \theta < 120°$ leads to estimations of friction that are not better than those resulting from the presently computed coarse grid pressure field. This is because only the pressure gradients are significant and they share similar girthwise values. On the leeside of this primary separation, there is again a strong increase of friction, the maximum of which, at $x/L = 0{\cdot}48$, $\theta \approx 160°$, is correlated to the local pressure peak. This explains the better behaviour of CFL3D and of the present fine grid results at this station, as an effect of an increased grid resolution.

Figures 6 and 7 present the comparisons between the computed wall skin friction lines and those reconstructed from experimental data. In contrast to the 10° case, the wall flow remains always divergent away from the leeside plane. It is interesting to note the good overall agreement with experiments of both models when the finer grid is used. However, a careful inspection of results indicates several differences. The first streamline convergence, for $x/L < 0{\cdot}2$, which is a characteristics of the flow at high incidences is predicted more leewards without corrections than with corrections,[14] while it is too weak with the coarse grid results. It will be seen that this result which occurs already in a zone where the flow is not yet turbulent is due to transition. The primary and secondary separation lines occur too early, i.e. too far from the leeside plane of symmetry, although the correction[14] improves their location with respect to the standard Baldwin–Lomax model.

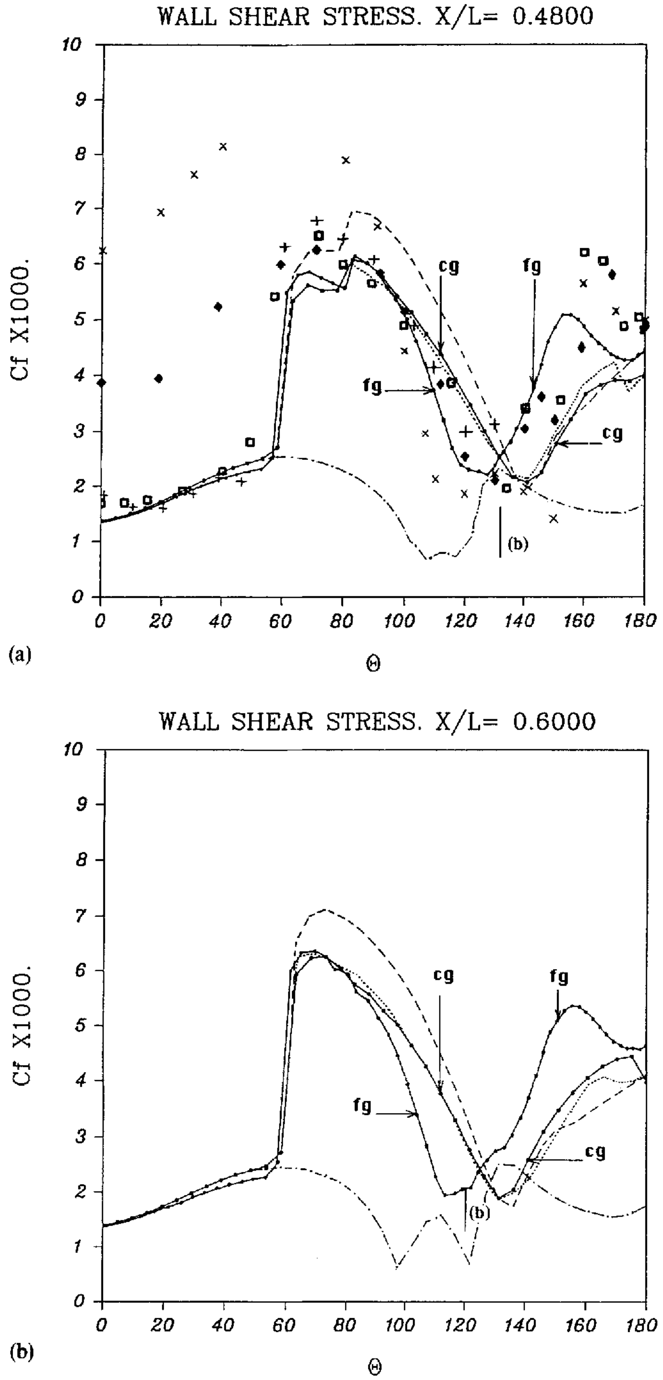

Figure 5. Girthwise distributions of the friction coefficient C_f for several x/L stations: (a) $x/L=0{\cdot}48$; (b) $x/L=0{\cdot}60$; (c) $x/L=0{\cdot}77$; (d) $x/L=0{\cdot}92$. $Re=7{\cdot}2\times10^6$; incidence 30°. □, C_f experimental data (taken from Reference 8 at $x/L=0{\cdot}48$ and Reference 10).———, present RANSE computations (the points indicate the location of grid points); Baldwin–Lomax model with modifications;[14] cg, coarse grid computation $70(\xi)\times40(\eta)\times40(\zeta)$; fg, fine grid computation: $120(\xi)\times60(\eta)\times60(\zeta)$. ...., present RANSE coarse grid computations; Baldwin–Lomax model without modifications.[14] – – – – –, present RANSE coarse grid computations; tanh model (3). – · – · – · –, present laminar flow computations. ◆, TLNS computations[10] with CFL3D. ×, TLNS computations[10] with VOR3DI. +, TBL results.[8] (b), breakdown of TBL calculations[8] due to separation

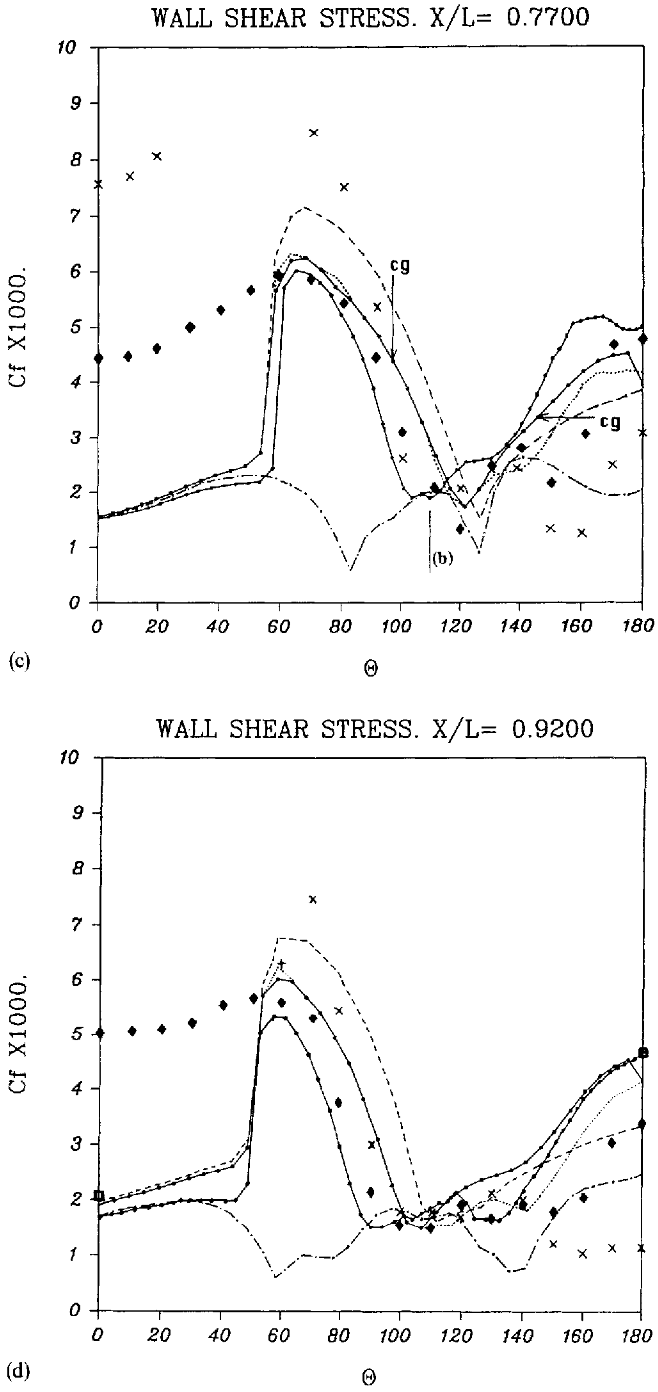

Figure 5. (Continued)

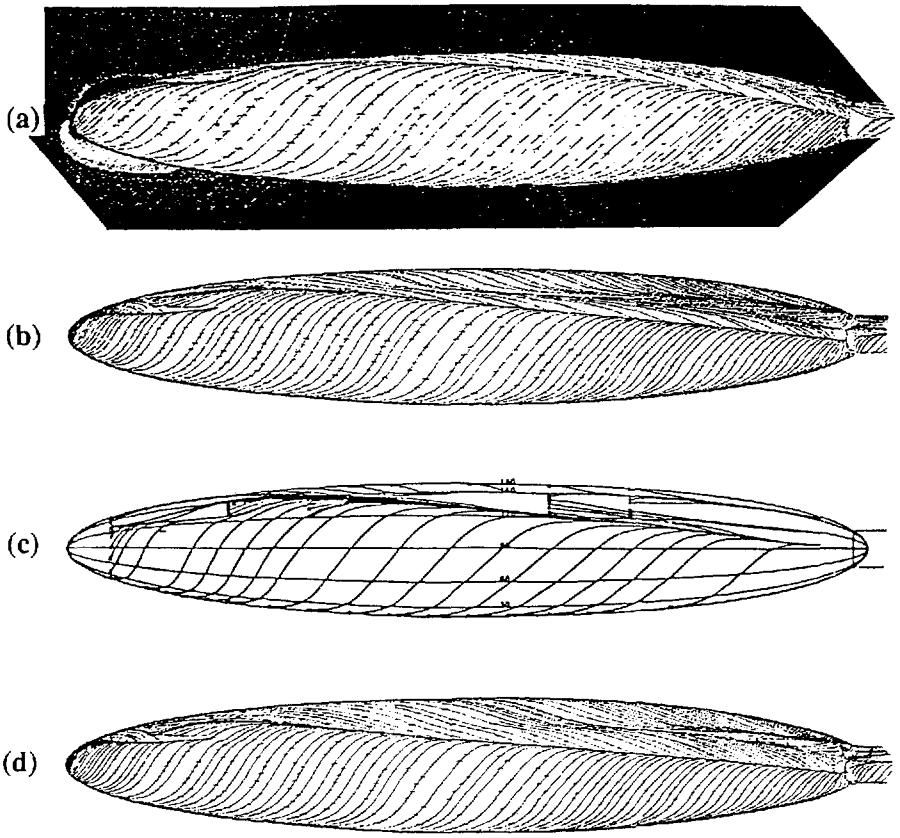

Figure 6. Comparison of skin friction lines reconstructed from experiments[2] with presently computed skin friction lines (transition switched on according to experiments). $Re=7\cdot2\times10^{6}$; incidence 30°. Side views. (a) coarse grid computation: $70(\xi)\times40(\eta)\times40(\zeta)$; Baldwin–Lomax model with modifications.[14] (b) fine grid computation: $120(\xi)\times60(\eta)\times60(\zeta)$; Baldwin Lomax model with modifications.[14] (c) skin friction lines reconstructed from experimental data; (d) fine grid computation $120(\xi)\times60(\eta)\times60(\zeta)$; Baldwin–Lomax model

In order to shed some light on the transition effects and on the flow separation mechanisms that are present, a view of the fore part of the spheroid is presented in Plate 2. The magnified view of the nose region (Plate 2(a)) details the vicinity of the forward stagnation point A which is located at $x_A/L=0\cdot65\times10^{-2}$. A is a nodal attachment point since all skin friction lines, but one (Aa) are tangent to the line $\theta=0$. The segment AN: $0\leqslant x/L\leqslant x_A/L$; $\theta=0$, is the locus of points where $|C_f|$ presents a girthwise local minimum so that $\partial|C_f|/\partial\theta=0$. From now, such a line is called a GSFmin line. There is another GSFmin line $\theta=\theta_s(x/L)$, Nu, which emanates from the nose along an angle $\theta_s(0)\approx138°$, passes through point U_0 ($x/L=57\times10^{-4}$; $\theta=153°$) where it is tangent to the skin friction line through U_0. It then moves towards downstream while remaining on the windward side of $\theta=166°7$ ($\zeta=53$). $|C_f|$ increases from A, where $|C_f|=0$, to the nose N and from N to U_0, where $|C_f|=6\cdot70\times10^{-3}$. Downstream of U_0, the GSFmin line crosses wall streamlines upstream of u, located somewhere about $I(=\xi)=18$, while the skin friction modulus decreases continuously until the point P_0 ($x/L\approx0\cdot1$; $\xi=24$; $\theta\approx125°$; $\zeta=35$), where $C_f\approx0\cdot52\times10^{-3}$, is reached (Plate 2(b)).

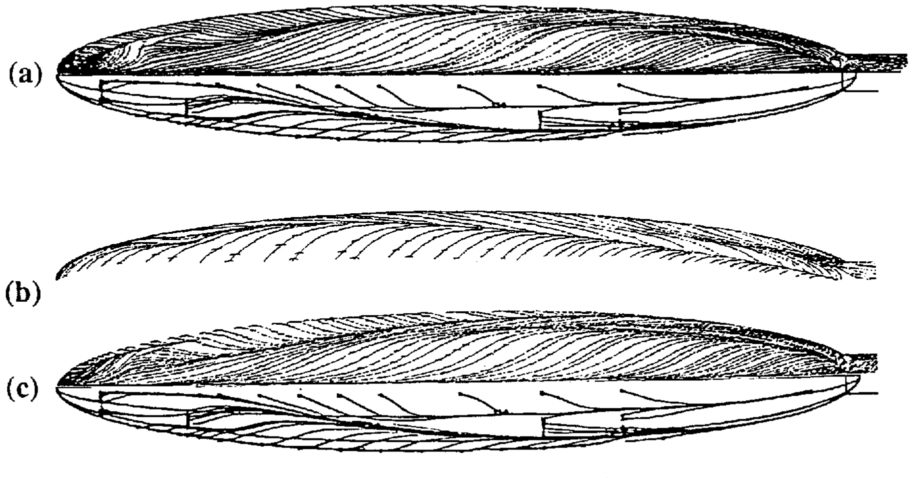

Figure 7. Comparison of skin friction lines reconstructed from experiments[2] with presently computed skin friction lines (transition switched on according to experiments). $Re = 7{\cdot}2 \times 10^6$; incidence 30°. Top views. (a) comparison between fine grid computation $120(\xi) \times 60(\eta) \times 60(\zeta)$; Baldwin–Lomax model (upper part) and skin friction lines reconstructed from experimental data (lower part). (b) Coarse grid computation; $70(\xi) \times 40(\eta) \times 40(\zeta)$; Baldwin–Lomax model with modifications.[14] (c) comparison between fine grid computation: $120(\xi) \times 60(\eta) \times 60(\zeta)$; Baldwin–Lomax model with modifications[14] (upper part) and skin friction lines reconstructed from experimental data (lower part).

Plate 2(b) presents a view of the skin friction vectors (in red) and of the skin friction lines (in black), somewhat away from the nose region. Wall streamlines that (all) emanate from the nodal point of attachment appear to focus along the GSFmin line, downstream of u. The GSFmin line is located in excellent agreement with the two experimental data points.[1] Downstream of P_0, that line is a local separation line (see e.g. Reference 23), being a particular limiting streamline that emanates from a nodal point of attachment. At its starting point, P_0, the skin friction modulus has a local minimum: $\partial|C_f|/\partial\theta = 0$, $\partial|C_f|/\partial x = 0$. Although the GSFmin line lies entirely in the laminar flow zone, it is clear that the flow pattern in this area is strongly affected by the transition line along which the turbulence is switched. Downstream of P_0, the GSFmin line becomes distinct from the local laminar separation (LLS) line and follows the line of inflexion points of wall streamlines, located slightly upstream of the transition line and parallel to it. The GSFmin line finally terminates at point P_1 ($x/L = 0{\cdot}41$; $\xi = 37$; $\theta = 65°$; $\zeta = 18$), where $|C_f| \approx 2{\cdot}35 \times 10^{-3}$ has a local minimum ($\partial|C_f|/\partial\theta = \partial|C_f|/\partial x = 0$), while the transition lines continues more downstream (Plate 2(c)) into a region where the normal velocity $\mathbf{V} \cdot \mathbf{N}$, close to the wall, is everywhere negative, as indicated by the blue colour. From now the streamwise and girthwise velocity components will be called U and W and be the contravariant components U^1 and U^3, respectively.

In contrast, the separation line suddenly bifurcates leewards into the turbulent zone. The abrupt bifurcation seems correlated to the fact that the normal velocity, close to the wall is positive upstream of P_0 (using the terminology,[24] the separation line is the trace on the wall of a negative bifurcation surface); and it becomes negative slightly downstream of P_0, as indicated by the transition red–blue (Plate 2(c)). The wall streamlines cross the transition ramp which is characterized by a convergence of the flow towards the wall and enter the main 'turbulence valley' which is now studied. How the bifurcation surface manages the 90°-turn of the separation line cannot be answered on the basis of the present grid resolution. Although hardly plausible, a singular behaviour (saddle-node?) for $25 \leqslant I \equiv \xi \leqslant 27$; $36 \leqslant K \equiv \zeta \leqslant 37$ cannot be discarded.

Another GSFmin line (V) emerges at point V_0 ($x/L \approx 0{\cdot}079$; $\xi = 22$; $\theta \approx 148°$; $\zeta = 45$), where $|C_f| \approx 1{\cdot}32 \times 10^{-3}$ and crosses the transition ramp which causes a strong increase of $|C_f|$ until point V$_1$ ($x/L\approx0{\cdot}127$; $\xi=25$; $\theta\approx150^{\circ}$; $\zeta=46$) where $|C_f|\approx3{\cdot}56\times10^{-3}$. While crossing wall streamlines, the GSFmin line enters a region where the flow converges towards the wall and the skin friction decreases slightly until point V$_2$ ($x/L\approx0{\cdot}208$; $\xi=29$; $\theta\approx157^{\circ}$; $\zeta=49$) where $|C_f|\approx2{\cdot}68\times10^{-3}$. V$_2$ is a local skin friction minimum ($\partial|C_f|/\partial\theta=\partial|C_f|/\partial x=0$) and, hence, a singular point. Following the valley (V), downstream of V$_2$, makes $|C_f|$ increase again until V$_3$ ($x/L\approx0{\cdot}25$; $\xi=31$; $\theta\approx151^{\circ}$; $\zeta=46$), where $|C_f|\approx2{\cdot}8\times10^{-3}$. Finally, $|C_f|$ decreases continuously downstream of V$_3$. For instance, at $x/L=0{\cdot}5$, $\xi=40$, $\theta\approx122^{\circ}$, $\zeta=35$, $|C_f|\approx2{\cdot}07\times10^{-3}$). The V-GSFmin line which is the bottom of this valley is, thus, the primary local turbulent separation (PLTS) line which starts from point V$_2$. Downstream of V$_2$, wall streamlines, including the streamline previously identified with the LLS line, converge towards the PLTS line. Point V$_3$ is characterized by the fact that the flow no longer diverges from the wall, along the PLTS line. Downstream of V$_3$, the PLTS line follows the line of vanishing normal velocity. It must be noticed that along both GSFmin lines, $\mathbf{V}\cdot\mathbf{N}$ passes from positive to negative values when θ increases. Also, the location of the V-GSF line is distant from experimental data[1] by at most one grid point in θ, i.e. by less than 3°.

A small $|C_f|$ valley (X) is present in the laminar zone but does not develop downstream because of the transition phenomenon. Instead, the corresponding GSFmin line starting at point X$_0$ ($x/L\approx0{\cdot}079$; $\xi=22$; $\theta\approx166^{\circ}7$; $\zeta=38$), where $|C_f|\approx1{\cdot}34\times10^{-3}$ terminates in the symmetry plane, at point X$_1$. Had the flow remained laminar, this valley (X) would have lead to a secondary separation line.

A second $|C_f|$ valley is present in the turbulent region. The corresponding GSFmin line (W) starts at point W$_0$ ($x/L\approx0{\cdot}25$; $\xi=31$; $\theta=173^{\circ}$; $\zeta=56$), where $|C_f|\approx4{\cdot}23\times10^{-3}$. The skin friction then decreases down to W$_1$($x/L\approx0{\cdot}385$; $\xi=36$; $\theta\approx173^{\circ}$; $\zeta=56$), where $|C_f|\approx4{\cdot}09\times10^{-3}$ is a local skin friction minimum ($\partial|C_f|/\partial\theta=\partial|C_f|/\partial x=0$). Again this GSFmin line is a (secondary) local turbulent separation line (SLTS line) downstream of W$_1$, along which the skin friction increases slowly with x/L. The main difference between the SLTS line and the PLTS line which lies along (V) is that the SLTS line is completely immersed in a zone where $\mathbf{V}\cdot\mathbf{N}<0$.

At last GSFmin line (Q) occurs in the windward symmetry plane, starting from the forward stagnation point A. (Q) is a line of divergence for the flow along which the skin friction increases from A to Q$_0$ ($x/L\approx0{\cdot}045$; $\xi=19$), where $|C_f|\approx1{\cdot}71\times10^{-2}$, and decreases from Q$_0$ to Q$_1$ ($x/L\approx0{\cdot}5$; $\xi=40$) where the skin friction is minimum: $|C_f|\approx1{\cdot}33\times10^{-2}$. However, the flow remaining divergent, Q$_1$ is not a starting point for a separation line.

To summarize the analysis, it has been shown that a consideration of GSFmin lines makes the understanding of the wall flow easier. (i) Such lines become local separation lines at points P$_0$, V$_2$, W$_1$ which are local skin friction minima. (ii) These local separation lines are either positive bifurcations: (W) or negative ones: (V) and (P). Upstream of the skin friction minima, the GSFmin lines pass through points U$_0$ or V$_1$ which can be called ‘passes’ (V$_3$ is also a ‘pass’) (see Figure 8(a)). (iii) While the GSFmin line (U) starts at the node A, where $|C_f|=0$, other GSF lines start at ‘semi-passes’ V$_0$ and W$_0$ (see Figure 8(a)). (iv) Convergence towards separation lines always occurs downstream of local $|C_f|$ minima P$_0$, V$_2$, W$_1$. (v) Upstream of these minima, wall streamlines cross GSFmin lines (U) and (W) through V$_0$V$_2$ and W$_0$W$_1$. (vi) However, the (P) GSFmin line is specific in that wall streamlines seem to focus towards it also upstream of P$_0$ while wall streamlines cross it only upstream of a point u which does not display any specificity. (vii) While the GSFmin line (U) terminates early at a ‘semi-pass’ P$_1$, other lines go far downstream.

Since two local turbulent separation lines emerge from the fore part of the spheroid, it is interesting to follow these lines and to investigate how they terminate. Plate 2(d) presents a magnified view of the spheroid junction zone with its sting support. Plate 2(e) is similar to Plate 2(c); however, grid points where $|\mathbf{V}\cdot\mathbf{N}|$ is close to zero ($<10^{-5}$) are now in green. The GSFmin

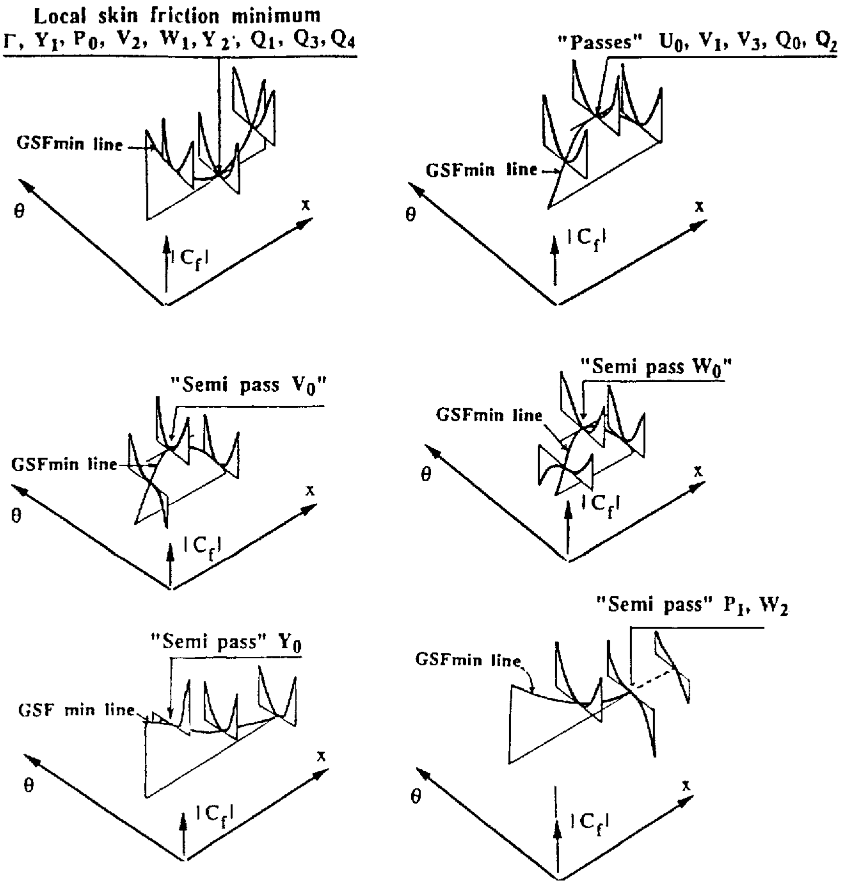

Figure 8(a). Schematic sketch of various points along the GSFmin lines

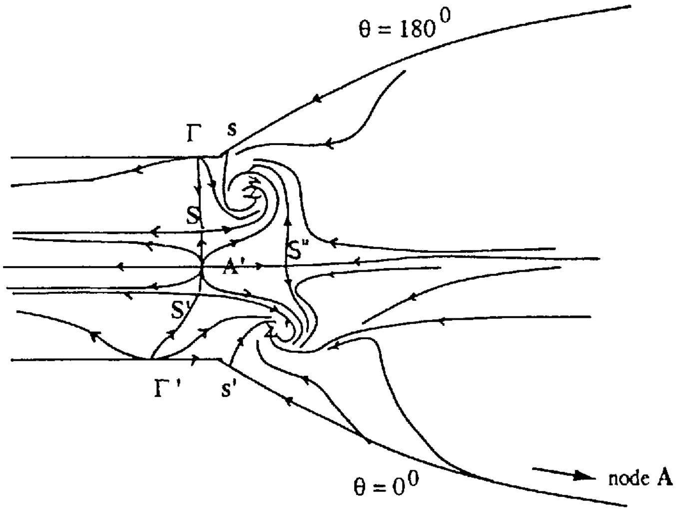

Figure 8(b). Overall topography of singular points over the prolate spheroid (flow from the right)

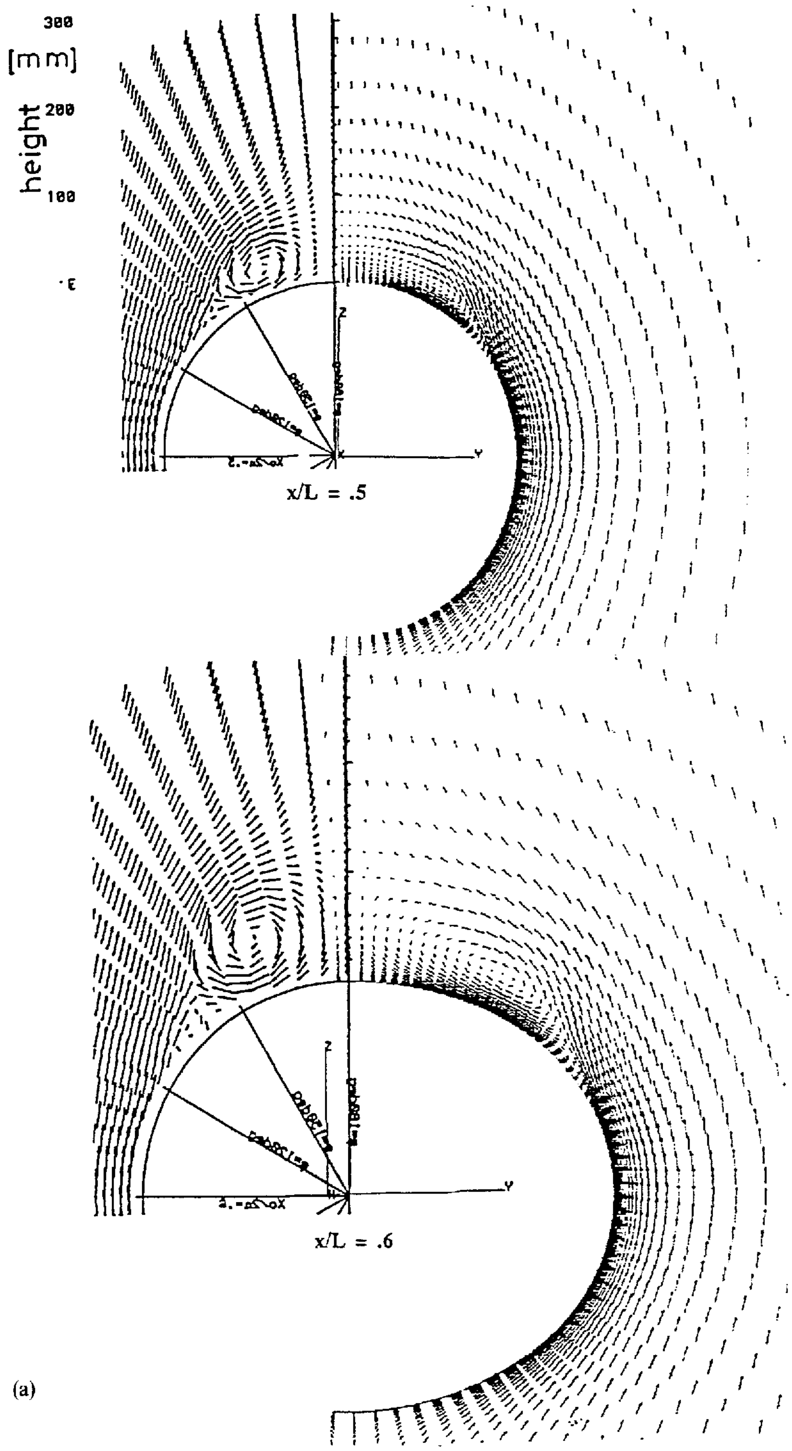

Figure 9. Comparison of secondary velocity plots in several transverse plane cross-sections: $x/L = 0{\cdot}5$, 0·6, 0·7, 0·8, 0·9 with available experimental data.[25] $Re = 7{\cdot}2 \times 10^6$; incidence 30°. Fine grid computation: $120(\xi) \times 60(\eta) \times 60(\zeta)$; Baldwin–Lomax model with modifications[14]

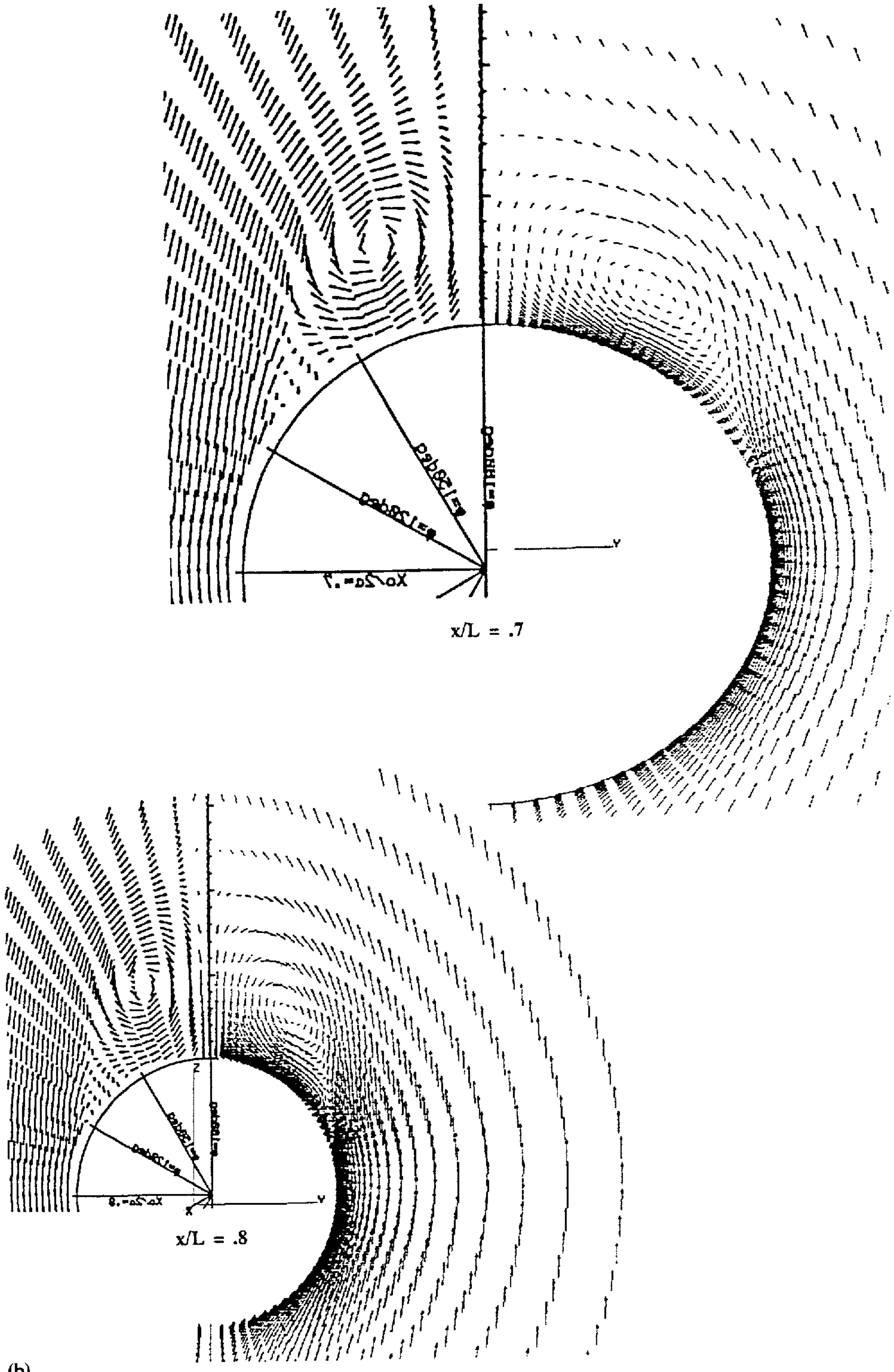

x/L = .7

x/L = .8

(b)

Figure 9. (Continued)

line (W), along which the secondary separation occurs, terminates at the semi-pass W_2 ($x/L=0{\cdot}916$, $\xi=66$, $\theta\equiv 175^\circ 6$, $\zeta=57$), where $|C_f|=4{\cdot}5\times 10^{-2}$, $W<0$ and $V<0$. More downstream, the flow clearly presents a saddle–node (focus) combination S–Σ related to the points of minimum skin friction (Plate 2(e)) Y_1 ($x/L=0{\cdot}974$, $\xi=72$, $\theta\equiv 138^\circ 3$, $\zeta=41$), where $|C_f|=0{\cdot}255\times 10^{-3}$, $W>0$ and $V\leqslant 0$ and Y_2 ($x/L=0{\cdot}986$, $\xi=74$, $\theta\equiv 133^\circ$, $\zeta=39$), where $|C_f|=0{\cdot}181\times 10^{-3}$, $W<0$ and $V\geqslant 0$, on either side of the flow reversal region (where U changes its sign). Points Y_1 and Y_2 are located on a GSFmin line (Y) starting at the semi-pass Y_0 ($x/L=0{\cdot}622$, $\xi=45$, $\theta\equiv 130^\circ 4$, $\zeta=38$). Y_2 is the starting point of the GSFmin line (Y′) which runs along the sting and coincides with the global separation line (Y′) emanating from S. The focal point Σ is about $\theta=166^\circ 7$; $x/L=0{\cdot}974$, while the saddle S is between 127° and 135°, rather close from $x/L\equiv 0{\cdot}98$. Another point of minimum skin friction occurs in the leeward symmetry point, at the junction $\theta=180^\circ$; $x/L=0{\cdot}78$, where $|C_f|\approx 3{\cdot}98\times 10^{-5}$, $W=0$, $V<0$. This point is a nodal point of attachment Γ located in the zone of flow reversal ($U<0$) and necessarily coupled slightly upstream to a saddle s, where $U=W=0$, also in the plane of symmetry.

Plate 2(d) indicates that another saddle-node pair S′–Σ′ is associated to the GSFmin line (V) which terminates in the region of flow reversal, at point V_4 ($x/L=0{\cdot}98$, $\xi=74$, $\theta\equiv 68^\circ 9$, $\zeta=19$), where $|C_f|\approx 1{\cdot}45\times 10^{-3}$, $U<0$, $V>0$, $W>0$. However, the topology is not as visible as on the leeside because of the lower vorticity level (also $\Delta\theta$ is higher here). The two side saddle-node pairs are connected by the node A′ located close to the starting point U'_0 of the GSFmin line (U') on the sting, i.e. in the region of flow reversal ($U<0$), close to $x/L\approx 0{\cdot}98$, $\xi=74$, $\theta\approx 110^\circ$; $\zeta=30$, where $|C_f|\approx 1{\cdot}2\times 10^{-3}$, $V<0$, $W\leqslant 0$.

The GSFmin line (Q), in the windward plane of symmetry, goes through the pass Q_2 ($x/L=0{\cdot}916$, $\xi=66$), where $|C_f|\approx 1{\cdot}69\times 10^{-2}$. Downstream of Q_1, $|C_f|$ decreases until two skin friction minima close to the boundary of the flow-reversal region which is slightly more developed than on the leeside. These friction minima are Q_3 ($x/L=0{\cdot}967$, $\xi=72$), where $|C_f|\approx 0{\cdot}82\times 10^{-2}$, $U\leqslant 0$, $V<0$, $W>0$ and Q_4 ($x/L=0{\cdot}9865$, $\xi=74$), where $|C_f|\approx 2{\cdot}6\times 10^{-3}$, $U\leqslant 0$, $V<0$, $W>0$. They indicate the presence of a saddle-node Γ′–s' pair in the plane of symmetry. The complete topography of singular points is summarized in Figure 8(b). It appears very similar, although somewhat more complex, than that proposed in Reference 24.

Secondary velocity plots, in surfaces $\xi=$constant corresponding to given wall values of $x/L=0{\cdot}5$, $0{\cdot}6$, $0{\cdot}7$, $0{\cdot}8$, are presented in Figure 9 with available corresponding experimental data.[25] Such results have been obtained using a bilinear interpolation of computed data in order to plot velocity arrows in surface cross-sections $\xi=$constant. Also the three-dimensional graphics software used for visualization makes it very difficult to provide a view angle in a direction strictly orthogonal to the spheroid, along its axis. For this reason, the cross-section is seen obliquely and appears as an ellipse. Although available experimental data are given in planes $x/L=$ constant, the overall agreement appears qualitatively correct. It will be noted, however, that the centre of the main vortex is slightly too close from the wall at $x/L=0{\cdot}5$, where the perspective effect and the surface distance (between the plane $x/L=0{\cdot}5$ and the surface $\xi=40$) are the weakest. This indicates that the wall divergence, away from the leeside plane of symmetry, is not intense enough. It is unfortunate that no velocity data are available, in order to quantify such differences.

5. CONCLUSION

A generally fully elliptic numerical method for the solution of RANSE has been developed and applied to the lifting flow past a prolate spheroid. The method uses a system of numerically generated curvilinear co-ordinates; it retains the Cartesian velocity components (as dependent variables), a non-staggered grid and a seggregated approach in which a pressure solver couples velocity and pressure fields, according to the so-called 'PISO' procedure. An LU-preconditioned conjugate gradient method improves the convergence of the pressure solver by an order of magnitude over standard relaxation techniques. The cpu computational effort per grid point is found to be roughly of $\sigma = 3 \times 10^{-2}$ s per grid point on Cray 2, for 444 iterations. This value of σ has already been cut down by a factor greater than two, due to a more adequate fortran optimization.[26] The following conclusions emerge from the study.

The main features of the vortical flows occuring at a high incidence are captured. The grid effect, however present, is far more important than in the low incidence case. It determines to a certain extent the quality of capture of girthwise pressure evolutions in the massively separated leeward region. A detailed comparison of pressure fields and shear stresses with available experimental data has been conducted. The existence of massive separation has been found to give rise to serious discrepancies with respect to experiments on the leeward side. In view of the well-known inability of turbulent models to account for massive separation, results can, however, be considered as satisfactory given the fact that the grid probably remains slightly too coarse both in the radial and in the circumferential direction. A detailed analysis of the flow topology has also been performed from the standpoint of the evolution of local $|C_f|$ minima in the girthwise direction. It has been confirmed that three local separation lines were present, one in the laminar zone which remains in the fore part of the spheroid, and two in the turbulent region which run along the whole spheroid. The overall flow topography of singular points in the aft part of the spheroid has been finally established.

ACKNOWLEDGEMENTS

Partial financial support of DRET, through contracts 86-104 and 89-117, is gratefully acknowledged. Thanks are also due to the Scientific Committee of CCVR and the DS/SPI for attributions of Cpu on the Cray 2 and on the VP200. Flow visualizations in Figures 6, 7, 9 and in Plates 1, 2(a)–(e) have been performed with the software 'ASCETE' from the CFD Group.

APPENDIX: NOMENCLATURE

$\mathbf{b}^i$	element area vector
C_p	pressure coefficient $(= -(p - p_\infty)/0{\cdot}5\,\rho U_\infty^2)$
g^{ij}	contravariant components of the metric tensor of the curvilinear co-ordinate system
J	Jacobian $D(x, y, z)/D(\xi, \eta, \zeta)$
k	turbulent kinetic energy
L	mixing length
n	local normal distance to the wall
p	pressure
$\mathscr{P}$, $\mathscr{U}$	unknowns of the model differential problem (12)
P	discrete approximation of pressure or of $\mathscr{P}$
Re	Reynolds number
s	local curvilinear abcissa along the wall streamline
$\mathbf{U}$	mean velocity vector
U	discrete approximation of $\mathscr{U}$
U^i	contravariant velocity components along ξ^i: $U^i = \mathbf{U} \cdot \mathbf{b}^i/J$
$\bar{U}^\alpha$	physical Cartesian $\bar{U}$, $\bar{V}$, $\bar{W}$ velocity components
$\overline{\mathbf{uu}}$	Reynolds stress

Greek symbols

τ	time step
ξ, η, ζ	curvilinear co-ordinates ξ^1, ξ^2, ξ^3, respectively

Subscripts and superscripts

C	central nodal points
i	index for contravariant components
n	actual discrete time
nb	symbolic notation for momentum stencil neighbours of point C (see equation (34), nb varies from 1 to 6 since the six nodal points U, D, E, W, N, S are involved)
NE, etc.	cardinal location of nodal points with respect to the current central station C
u, d	upstream, downstream facets (along ξ) of the mass control volume.
U, D	upstream, downstream nodal points, other involved nodal points: N, S (along η); E, W (along ζ)
α	index for Cartesian components

REFERENCES

1. H. U. Meier and H. P. Kreplin, 'Experimental investigation of the boundary layer transition and separation on a body of revolution', *Z. Flugwiss. Weltraumforsch.*, **4**(2), 65–71 (1980).
2. H. P. Kreplin, H. Vollmers and H. U. Meier, 'Measurements of the wall-stress on an inclined prolate spheroid', *Z. Flugwiss. und Weltraumforsch.*, **6**(4), 248–252 (1982).
3. H. U. Meier, H. P. Kreplin and H. Vollmers, Development of boundary layers and separation patterns on a body of revolution at incidence', *Proc. 2nd. Symp. Num. Phys. Aspects of Aerodynamic Flows*, Long Beach, California, 1983.
4. H. U. Meier, H. P. Kreplin and H. Vollmers, 'Velocity distributions in threedimensional boundary layers and vortex flows developing on an inclined prolate spheroid ', *DFVLR-AVA-Report IB 222 81 CP 1*, 1981.
5. J. Piquet and P. Queutey, 'Navier Stokes computations past a prolate spheroïd at incidence. I. Low incidence case', *Comput. Fluids* (1992) (to appear).
6. S. A. Ragab, 'A method for the calculation of three-dimensional boundary layers with circumferential reversed flow on bodies', *AIAA Paper 82-1023*, 1982.
7. T. Cebeci, 'Problems and opportunities with threedimensional boundary layers', *AGARD R 719; Three Dimensional Boundary Layers*, 1984.
8. S. A. Ragab, 'Steady and unsteady boundary layer on prolate spheroids at high incidence', *AIAA 85-1708*, 1985.
9. V. N. Vatsa, J. L. Thomas and B. W. Wedan, 'Navier–Stokes computation of prolate spheroids at angle of attack', *J. Aircraft*, **26**, 986–993 (1989). See also *AIAA 87-2627-CP*, 1987.
10. T. C. Wong, O. A. Kandil and C. H. Liu, 'Navier–Stokes computation of separated vortical flows past prolate spheroid at incidence', *AIAA 89-0553*, 1989.
11. V. N. Vatsa, 'Flow over prolate spheroïds at incidence', *Comput. Fluids*, **20**, 313–320 (1991).
12. P. M. Hartwich and R. M. Hall, 'Navier–Stokes solutions for vortical flows over a tangent-ogive-cylinder', *AIAA Paper 89-0337*, 1989.
13. B. S. Baldwin and H. Lomax, 'Thin-layer approximation and algebraic model for separated turbulent flows', *AIAA Paper 78-257*, 1978.
14. D. Degani and L. B. Schiff, 'Computation of turbulent supersonic flows around pointed bodies having crossflow separation', *J. Comput. Phys.*, **66**, 173–196 (1986).
15. J. E. Thompson, Z. U. A. Warsi and C. W. Mastin, *Numerical Grid Generation, Foundations and Applications*, North Holland Publishers, N.Y., 1985.
16. G. E. Schneider and M. J. Raw, 'Control volume finite element method for heat transfer and fluid flow using colocated variables', *Numer. Heat Transfer*, **11**, 363–400 (1987).
17. C. M. Rhie and W. L. Chow, 'A numerical study of the turbulent flow past an isolated airfoil with trailing edge separation', *AIAA-82-0998*, 1982.
18. R. I. Issa, 'Solution of the implicitly discretised fluid flow equations by operator-splitting', *J. Comput. Phys.*, **62**, 40–65 (1985).
19. J. Piquet and M. Visonneau, 'Computation of the flow past a shiplike hull', *Comput. Fluids*, **19**, 183–215 (1991).
20. V. C. Patel and J. H. Baek, 'Boundary layers in planes of symmetry, Part II: calculations for laminar and turbulent flows', *AIAA J.*, **25**, 812–818 (1987).
21. H. Schmidt, 'Potential and thin-layer flow about a prolate spheroid', *Z. Flugwiss. Weltraumforsch.*, **14**, 117–119 (1990).

22. D. P. Telionis and C. E. Costis, 'Three-dimensional separation and vortical wakes over a prolate spheroid', *DTNSRDC-ASED-CR-01-85 Report*, AD-A164 781, 1985.
23. M. Tobak and D. J. Peake, 'Topology of three-dimensional separated flows', *Ann. Rev. Fluid Mech.*, **14,** 61–86 (1982).
24. H. Hornung and A. E. Perry, 'Some aspects of three-dimensional separation, Part 1: streamsurface bifurcations', *Z. Flugwiss. Weltraumforsch.*, **8,** 77–87 (1984).
25. H. Vollmers, H. U. Meier and H. P. Kreplin, 'Separation and vortical type flow around a prolate spheroid–evaluation of relevant parameters', *AGARD-FDP-CP 342*, 14.1–14.14, 1983.
26. G. B. Deng, G. Guilmineau, P. Queutey and M. Visonneau, 'Numerical simulation of unsteady laminar viscous 3D flows', *GAMM Workshop on Numerical Simulation of 3-D Incompressible Unsteady Viscous Laminar Internal and/or External Flows.* Paris, 1992, (to appear).